J Pharmacol Sci 96, 23 – 26 (2004)

Journal of Pharmacological Sciences

Forum Minireview

Forefront of Na^+/Ca^{2+} Exchanger Studies: Role of Na^+/Ca^{2+} Exchanger – Lessons From Knockout Mice

Issei Komuro[1,*] and Masashi Ohtsuka[1]

[1]*Department of Cardiovascular Science and Medicine, Chiba University Graduate School of Medicine, 1-8-1 Inohana, Chuo-ku, Chiba 260-8670, Japan*

Received June 14, 2004; Accepted July 27, 2004

Abstract. We used Na^+/Ca^{2+} exchanger (NCX) knockout mice to evaluate the effects of NCX in cardiac function and the infarct size after ischemia/reperfusion injury. The contractile function in NCX KO mice hearts was significantly better than that in wild type (WT) mouse hearts after ischemia/reperfusion and the infracted size was significantly smaller in NCX KO mice hearts compared with that in WT mice hearts. NCX is critically involved in the development of ischemia/reperfusion-induced myocardial injury, and therefore the inhibition of NCX function may contribute to cardioprotection against ischemia/reperfusion injury.

Keywords: Na^+/Ca^{2+} exchanger (NCX), knockout mouse, heart, ischemia/reperfusion injury

Introduction

The Na^+/Ca^{2+} exchanger (NCX) is an important electrogenic transporter in maintaining calcium homeostasis in a variety of mammalian organs (1). NCX catalyzes electrogenic exchange of Na^+ and Ca^{2+} across the plasma membrane in either the Ca^{2+}-efflux (the forward mode) or Ca^{2+}-influx (the reverse mode), depending on the electrochemical gradients of the substrate ions. In the heart, NCX plays an important role in excitation-contraction coupling as the dominant myocardial Ca^{2+}-efflux system (2). On the other hand, the reverse mode of NCX is associated with in cytoplasmic Ca^{2+} levels in cardiomyocytes during digitalis treatment or ischemia/reperfusion (3). It has been reported that NCX inhibitors and NCX antisense oligonucleotides protect the heart from ischemia/reperfusion injury (4, 5). However, two putative NCX inhibitors, KB-R7943 and SEA0400, have been reported to be not specific for NCX (6). Therefore, it remains unclear whether NCX indeed plays a crucial role in mediating Ca^{2+} influx that leads to Ca^{2+} overload and cellular injury after myocardial ischemia, reperfusion injury.

We generated *Ncx1*-deficient mice by gene targeting to determine the in vivo function of the exchanger (7). Homozygous *Ncx1*-deficient mice died between embryonic days 9 and 10. Their hearts did not beat, and cardiac myocytes showed apoptosis. No forward mode or reverse mode of the Na^+/Ca^{2+} exchange activity was detected in null mutant hearts. The Na^+-dependent Ca^{2+} exchange activity as well as protein content of NCX1 were decreased by approximately 50% in the heart, kidney, aorta, and smooth muscle cells of the heterozygous mice, and tension development of the aortic ring in Na^+-free solution was markedly impaired in heterozygous mice. These findings suggest that NCX1 is required for heartbeats and survival of cardiac myocytes in embryos and plays critical roles in Na^+-dependent Ca^{2+} handling in the heart and aorta.

*Corresponding author. FAX: +81-43-226-2557
E-mail: komuro-tky@umin.ac.jp

The functional activity as well as the protein content of NCX in the myocardium of NCX KO mice is approximately half of those of WT mice

Twelve-week-old male heterozygous knockout (KO) mice and wild type (WT) littermates were used. All animal experiments were performed according to the Guide for the Care and Use of Laboratory Animals (NIH publication No. 85-23, revised 1996). Ventricular cells were prepared from adult mouse hearts by standard enzymatic digestion (8). Whole-cell membrane currents were recorded by the patch-clamp method and the current-voltage relationship was obtained by voltage clamp ramp pulses as described previously (9). Under

these conditions, the Ni^{2+}-sensitive current represents NCX current (10). All data were acquired and analyzed by the pCLAMP (version 5.5; Axon Instrument) software.

Expression levels of dihydropyridine (DHP) receptor (L-type Ca^{2+} channel) and SR Ca^{2+}-ATPase 2 (SERCA2) were analyzed by Western blot as described previously (11). Briefly, tissue was homogenized in lysis buffer containing 25 mM Tris-HCl (pH 7.4), 25 mM NaCl, 0.5 mM EGTA, 10 mM sodium pyrophosphate, 1 mM sodium orthovanadate, 10 mM NaF, 10 nM okadaic acid, 1 mM PMSF, 20 μg/ml aprotinin, and 20 μg/ml leupeptin. Protein concentration was determined using a protein assay kit (BioRad, Hercules, CA, USA) and equal amounts of total protein (40 μg/lane) were separated on 8% SDS-polyacrylamide gel. Separated proteins were transferred to nitrocellulose membrane (Amersham Life Science, Arlington Heights, IL, USA). Membranes were incubated with anti-mouse dihydropyridine L-type Ca^{2+} channel α-2 subunit monoclonal antibody (Affinity Bioreagents, Inc., Golden, CO, USA) or anti-mouse SERCA2 monoclonal antibody (Affinity Bioreagents) at 4°C overnight. After washing, the membranes were incubated with horseradish peroxidase-conjugated goat anti-mouse antibody for 1 h. Immunoreactive protein was visualized using an enhanced chemiluminescence detection kit (ECL, Amersham).

We previously reported that the protein content of NCX in NCX KO mouse hearts was approximately 50% of that in WT mouse hearts (12). To elucidate the functional activity, we examined NCX current densites from −40 mV to 40 mV in WT (n = 9) and NCX KO ventricular cells (n = 6) (Fig. 1). The densities of the reverse mode of NCX at 40 mV in ventricular cells of KO mice (0.57 ± 0.07 pA/pF) were approximately half (55.4%) compared with those of WT mice (1.04 ± 0.14 pA/pF). These results suggest that the functional activity as well as the protein content of NCX in the myocardium of NCX KO mice is approximately half of those of WT mice.

Western blot analysis revealed that there was no difference in the protein levels of L-type Ca^{2+} channel and SERCA2 between the two groups (data not shown).

The infarct size was significantly smaller in KO hearts than in WT hearts

Hearts were excised from mice and connected to the perfusion canula via the aorta as described previously (8). Retrograde perfusion was maintained with Krebs-Henseleit solution. To evaluate the contractile function, a polyethylene film balloon was inserted into the cavity of the left ventricle through the left atrium. The balloon was filled with saline to adjust the baseline end-diastolic pressure to 5 – 10 mmHg. Hearts were subjected to no-flow, global ischemia by clamping the perfusion line. After 30 min of ischemia, the clamp was released and the hearts were reperfused for 120 min. Left ventricular developed pressure (LVDP) was designated as difference between systolic and diastolic pressures of the left ventricle. After 120 min, the heart was incubated for 5 min at 37°C in a 1% solution of triphenyltetrazolium chloride (TTC). The sizes of the infarcted area and viable ischemic-reperfused area were measured by computed planimetry (Scion Image 1.62; Scion Corporation, Frederick, MD, USA). Infarct size was calculated as described previously (13).

There were no significant differences in the basal hemodynamic parameters, including heart rate, left ventricular pressure, end-diastolic pressure, and positive and negative dP/dt, between WT and KO mice (Table 1). After ischemia, there was no significant difference between the two groups in several parameters such as time to no beating, time to contracture, and left

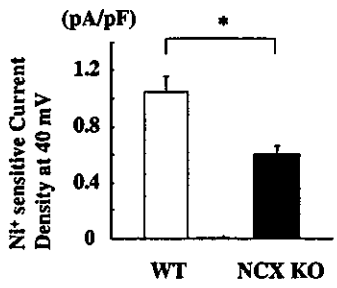

Fig. 1. NCX current densities. The densities of the reverse mode of NCX at 40 mV in ventricular myocytes isolated from WT (n = 9) and NCX KO mice hearts (n = 6). Values are expressed as the mean ± S.E.M. *P<0.05 *vs* WT mice.

Table 1. Hemodynamic parameters of NCX KO mice

	WT (n = 6)	NCX KO (n = 7)
HR (bpm)	356 ± 40	378 ± 77
LVP (mmHg)	142.8 ± 40	146.3 ± 34.5
EDP (mmHg)	4.4 ± 1.5	4.3 ± 1.3
dP/dt (mmHg/s)	7368 ± 630	7845 ± 2582
−dP/dt (mmHg/s)	5204 ± 782	5539 ± 1157
Time to no beating (min)	2.2 ± 0.9	2.2 ± 1.6
Time to contracture (min)	6.2 ± 1.7	6.3 ± 2.0
EDP at 25 min (mmHg)	67.3 ± 9.2	63.8 ± 10.8

HR, heart rate; LVP, left ventricular pressure; EDP, LV end-diastolic pressure; dP/dt and −dP/dt, positive and negative first derivatives for maximal rates of LV pressure development, respectively.

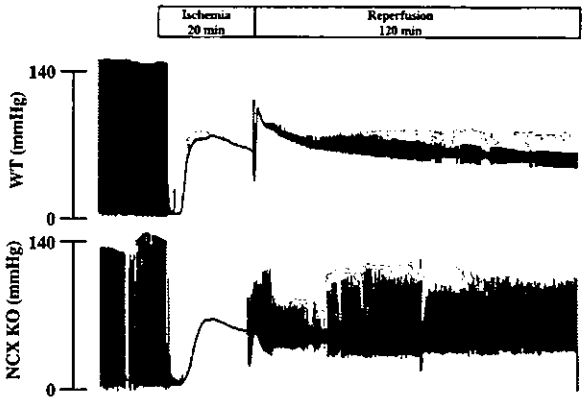

Fig. 2. Ex vivo studies. Changes in LVP during ischemia/reperfusion. Representative LVP records of WT and NCX KO mouse hearts are shown. Note that KO mouse hearts started to contract earlier than WT mouse hearts after reperfusion.

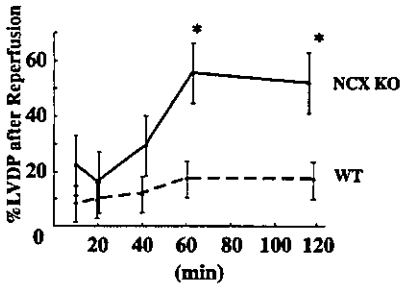

Fig. 3. LVDP of hearts of NCX KO mice (n = 7) and WT mice (n = 6) hearts after reperfusion. Values are expressed as the mean ± S.E.M. *$P<0.05$ *vs* WT mice.

ventricular end-diastolic pressure (Fig. 2). After reperfusion, however, hearts of KO mice started to beat earlier than those of WT mice (Fig. 2). At 120 min after reperfusion, contractile function (left ventricular developed pressure) of KO mouse hearts was significantly better (51.7 ± 12.7% of preischemic value) than that of WT mouse hearts (26.3 ± 6.9%, $P<0.05$) (Fig. 3). After ischemia/reperfusion, there was much more viable myocardium in KO hearts than WT hearts (red lesion (printed in black) in Fig. 4A). The infracted size was significantly smaller in KO hearts (32 ± 9%) than in WT hearts (68 ± 10%, $P<0.05$) (white lesion in Fig. 4A and Fig. 4B).

Concluding remarks

Myocardial cell injury is induced by a combination of mechanical and chemical stresses during ischemia

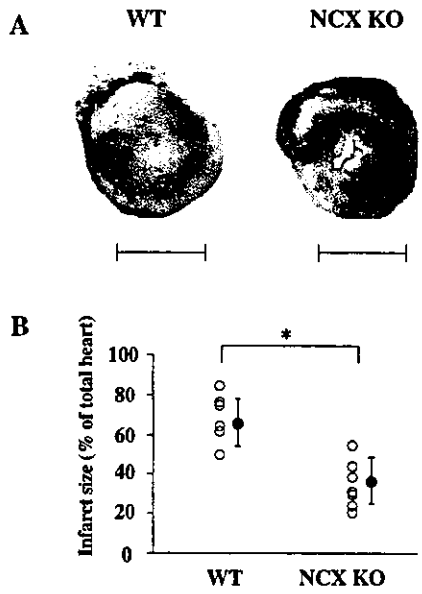

Fig. 4. Infarct size. A: Representative TTC staining photographs of WT and NCX KO mice hearts after ischemia/reperfusion are shown. Infarct area is expressed as a white lesion and viable myocardium is expressed as a red lesion (printed in black). Bar = 2 mm. B: Myocardial infarct size is expressed as percentage for the total heart of WT mice (n = 6) and NCX KO mice (n = 7). Values are expressed as the mean ± S.E.M. *$P<0.05$ *vs* WT mice.

(14). Reoxygenation after extended periods of ischemia rapidly induce hypercontracture of cardiomyocytes (15) and aggravate the preexisting injury (16). The hypercontracture represents a major cause of acute lethal cell injury in the reperfused myocardium (17, 18). It has been hypothesized that an increase in intracellular Ca^{2+} levels of cardiomyocytes through NCX induces the hypercontracture state after reperfusion but not during ischemia by the mechanism described below (5). During myocardial ischemia, anaerobic metabolism induces acidosis both inside and outside of cardiomyocytes. The Na^+/H^+ exchanger does not operate at this moment because of no difference in H^+ concentration across the plasma membrane of cardiomyocytes. Reperfusion restores extracellular acidosis, leading to a disparity in H^+ concentration between the inside and outside of cardiomyocytes. The increase in intracellular H^+ concentration activates the Na^+/H^+ exchanger, and the elevated intracellular Na^+ concentration triggers a rise in intracellular Ca^{2+} by the reverse mode of NCX (5). The excessive Ca^{2+} overload induces the catastrophic hypercontracture of cardiomyocytes. In fact, it has been reported that reduction of Ca^{2+} concentration protects cardiomyocytes against hypercontracture evoked by reoxygenation (19). In contrast, overexpression of NCX

increased ischemia/reperfusion injury in mice (20). Pharmacological inhibition of reverse mode of NCX protected reperfusion injury in cardiomyocytes (19). These results suggest that NCX is critically involved in the myocardial ischemia/reperfusion injury; however, NCX inhibitors have been recently reported to be not specific to NCX (6). Two putative NCX inhibitors, KB-R7943 and SEA0400, depressed the Ca^{2+} transients even in cardiomyocytes of NCX null mice (7). Although these NCX inhibitors have been reported to suppress the reverse mode but not the forward mode of NCX, the administration of high dose of these inhibitors increased infarct size possibly by inhibiting the forward mode of NCX (21). We here demonstrated an important role of NCX in myocardial ischemia/reperfusion injury by using NCX KO mice. The reverse mode of NCX current in KO mice was decreased to half that of WT mice. Loss of function of NCX is assumed to result in alleviation of Ca^{2+} overload, hypercontracture, and cell death after reperfusion. Our present study clearly indicates that the inhibition of NCX contributes to cardioprotection against myocardial ischemia/reperfusion injury and suggests that specific inhibitors of the reverse mode of NCX may be useful to prevent the myocardial ischemia/reperfusion inury.

Acknowledgments

We thank to Y. Reien for the current density analysis and R. Kobayashi, E. Fujita, M. Watanabe, M. Iida, and A. Ohkubo for technical assistance. This work was supported in part by grants from the Japanese Ministry of Education, Culture, Sports, Science, and Technology and the Japan Health Sciences Foundation.

References

1 Schulze D, Kofuji P, Hadley R, Kirby MS, Kieval RS, Doering A, et al. Sodium/calcium exchanger in heart muscle: molecular biology, cellular function, and its special role in excitation-contraction coupling. Cardiovasc Res. 1993;27:1726–1734.

2 Bridge JH, Smolley JR, Spitzer KW. The relationship between charge movements associated with I_{Ca} and $I_{Na\text{-}Ca}$ in cardiac myocytes. Science. 1990;248:376–378.

3 Kleber AG. Resting membrane potential, extracellular potassium activity, and intracellular sodium activity during acute global ischemia in isolated perfused guinea pig hearts. Circ Res. 1983; 52:442–450.

4 Pilitsis JG, Diaz FG, O'Regan MH, Phillis JW. Inhibition of Na^+/Ca^{2+} exchange by KB-R7943, a novel selective antagonist, attenuates phosphoethanolamine and free fatty acid efflux in rat cerebral cortex during ischemia-reperfusion injury. Brain Res. 2001;916:192–198.

5 Eigel BN, Hadley RW. Antisense inhibition of Na^+/Ca^{2+} exchange during anoxia/reoxygenation in ventricular myocytes. Am J Physiol Heart Circ Physiol. 2001;281:H2184–H2190.

6 Reuter H, Henderson SA, Han T, Matsuda T, Baba A, Ross RS, et al. Knockout mice for pharmacological screening: testing the specificity of Na^+/Ca^{2+} exchange inhibitors. Circ Res. 2002; 91:90–92.

7 Wakimoto K, Kobayashi K, Kuro OM, Yao A, Iwamoto T, Yanaka N, et al. Targeted disruption of Na^+/Ca^{2+} exchanger gene leads to cardiomyocyte apoptosis and defects in heartbeat. J Biol Chem. 2000;275:36991–36998.

8 Suzuki M, Li RA, Miki T, Uemura H, Sakamoto N, Ohmoto-Sekine Y, et al. Functional roles of cardiac and vascular ATP-sensitive potassium channels clarified by Kir 6.2-knockout mice. Circ Res. 2001;88:570–577.

9 Watanabe Y, Kimura J. Inhibitory effect of amiodarone on Na^+/Ca^{2+} exchange current in guinea-pig cardiac myocytes. Br J Pharmacol. 2000;131:80–84.

10 Kimura J, Miyamae S, Noma A. Identification of sodium-calcium exchange current in single ventricular cells of guinea-pig. J Physiol (Lond). 1987;384:199–222.

11 Zou Y, Komuro I, Yamazaki T, Kudoh S, Uozumi H, Kadowaki T, et al. Both Gs and Gi proteins are critically involved in isoproterenolinduced cardiomyocyte hypertrophy. J Biol Chem. 1999;274:9760–9770.

12 Takimoto E, Yao A, Toko H, Takano H, Shimoyama M, Sonoda M, et al. Sodium calcium exchanger plays a key role in alteration of cardiac function in response to pressure overload. FASEB J. 2002;16:373–378.

13 Suzuki M, Sasaki N, Miki T, Sakamoto N, Ohmoto-Sekine Y, Tamagawa M, et al. Role of sarcolemmal K(ATP) channels in cardioprotection against ischemia/reperfusion injury in mice. J Clin Invest. 2002;109:509–516.

14 Piper HM, Garcia-Dorland D, Ovize M. A fresh look at reperfusion injury. Cardiovasc Res. 1998;38:291–300.

15 Siegmund B, Koop A, Klietz T, Schwartz P, Piper HM. Sarcolemmal integrity and metabolic competence of cardiomyocytes under anoxiareoxygenation. Am J Physiol. 1990;258: H285–H291.

16 Stern MD, Chien AM, Capogrossi MC, Pelto DJ, Lakatta EG. Direct observation of the "oxygen paradox" in single rat ventricular myocytes. Circ Res. 1985;56:899–903.

17 Barrabes JA, Garcia-Dorado D, Ruiz-Meana M, Piper HM, Solares J, Gonzalez MA, et al. Myocardial segment shrinkage during coronary reperfusion in situ. Relation to hypercontracture and myocardial necrosis. Pflugers Arch. 1996;431:519–526.

18 Ganote CE. Contraction band necrosis and irreversible myocardial injury. J Mol Cell Cardiol. 1983;15:67–73.

19 Schafer C, Ladilov Y, Inserte J, Schafer M, Haffner S, Garcia-Dorado D, et al. Role of the reverse mode of the Na^+/Ca^{2+} exchanger in reoxygenation-induced cardiomyocyte injury. Cardiovasc Res. 2001;51:241–250.

20 Cross HR, Lu L, Steenbergen C, Philipson KD, Murphy E. Overexpression of the cardiac Na^+/Ca^{2+} exchanger increases susceptibility to ischemia/reperfusion injury in male, but not female, transgenic mice. Circ Res. 1998;83:1215–1223.

21 Inserte J, Garcia-Dorado D, Ruiz-Meana M, Padilla F, Barrabes J, Pina P, et al. Effect of inhibition of Na^+/Ca^{2+} exchanger at the time of myocardial reperfusion on hypercontracture and cell death. Cardiovasc Res. 2002;55:739.

Double Aortic Arch With a Compressed Trachea Demonstrated by Multislice Computed Tomography

Nobusada Funabashi, MD; Atsushi Ishida, MD; Katsuya Yoshida, MD; Issei Komuro, MD

A 33-year-old man had a chest x-ray that showed an abnormal enlargement of the thoracic aorta. ECG-gated enhanced multislice computed tomography (CT) (Light Speed Ultra 16, General Electric) was therefore performed with a 0.625-mm slice thickness and a helical pitch of 3.25. Thirty seconds after intravenous injection of 100 mL of iodinated contrast material (350 mgI/mL), CT scanning was performed with retrospective ECG-gated reconstruction and volume data were transferred to a workstation (Virtual Place Office, Azemoto, Tokyo, Japan).

Axial source images (Figure 1A) and multiplanar reconstruction images of the coronal view (Figure 1B) revealed separated right and left aortic arches and a trachea and esophagus surrounded by a vascular ring made by the double aortic arches. The trachea was actually slightly compressed by the vascular ring (Figure 1B, arrowhead). Three-dimensional volume rendering images also revealed the double aortic arch, which was separated at the distal portion of the ascending aorta (Figure 2A) and joined at the proximal portion of the descending aorta (Figure 2B). The right subclavian artery and right common carotid artery both originated separately from the right aortic arch, and the left subclavian artery and left common carotid artery originated from the left aortic arch. Because the patient did not experience symptoms of compression of the esophagus or trachea, surgical intervention is not currently planned.

Acknowledgments

This work was supported by Japan Cardiovascular Research Foundation.

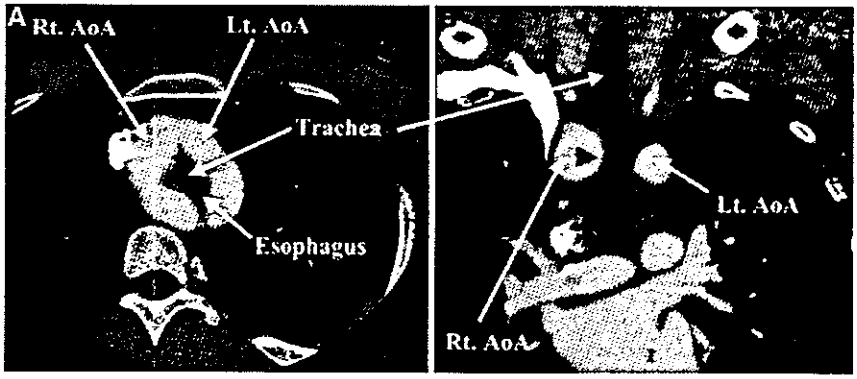

Figure 1. Axial source image (A) and multiplanar reconstruction image from the coronal view (B) of enhanced multislice CT revealed separate right (rt.) and left (lt.) aortic arches (AoA). The trachea and esophagus were surrounded by a vascular ring made by the double AoA (A), and the trachea was actually slightly compressed by the vascular ring (B, arrowheads).

From the Departments of Cardiovascular Science and Medicine (N.F., K.Y., I.K.) and General Surgery (A.I.), Chiba University Graduate School of Medicine, Chiba, Japan.

Correspondence to Issei Komuro, MD, Department of Cardiovascular Science and Medicine, Chiba University Graduate School of Medicine, 1-8-1 Inohana, Chuo-ku, Chiba City, Chiba 260-8670, Japan. E-mail komuro-tky@umin.ac.jp

(*Circulation.* 2004;110:e68-e69.)

Circulation is available at http://www.circulationaha.org

DOI: 10.1161/01.CIR.0000138742.98726.5F

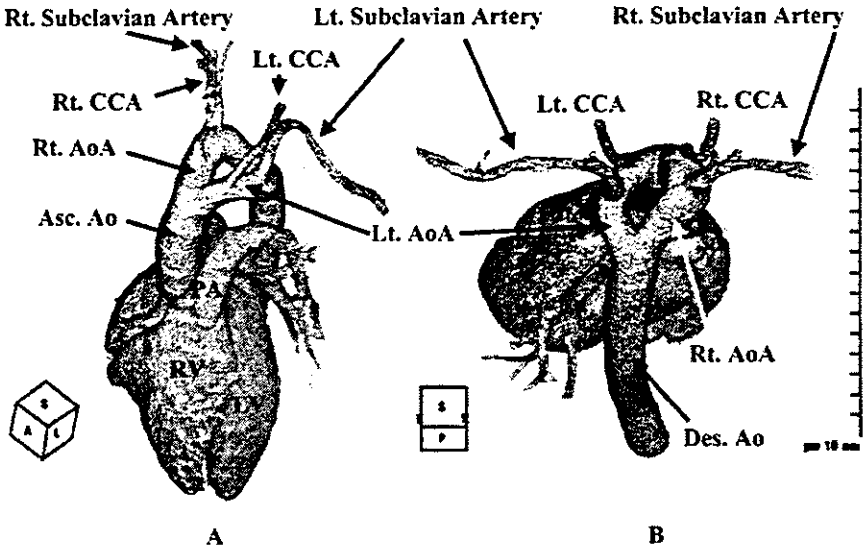

Figure 2. Three-dimensional volume rendering image of enhanced multislice CT from the left superior anterior view (A) and from the superior posterior view (B) revealed double aortic arches (AoA) separated at the distal portion of the ascending aorta (Asc. Ao) (A) and joined at the proximal portion of the descending aorta (Des. Ao) (B). The right (rt.) subclavian artery and right common carotid artery (CCA) originated separately from the right aortic arch (rt. AoA), and the left (lt.) subclavian artery and left CCA originated from the left aortic arch (lt. AoA). PA indicates pulmonary artery; RV, right ventricle; and LV, left ventricle.

Circ J 2004; **68:** 769–777

New Method of Measuring Coronary Diameter by Electron-Beam Computed Tomographic Angiography Using Adjusted Thresholds Determined by Calibration With Aortic Opacity

Nobusada Funabashi, MD; Yoshiki Kobayashi, MD*; Masayuki Kudo, RT**; Miki Asano, MT; Kiyomi Teramoto, MD; Issei Komuro, MD; Geoffrey D Rubin, MD†

Background In a previous study the adjusted thresholds at which the diameters of coronary arteries determined by enhanced electron-beam computed tomography (CT) scans are equal to the corresponding quantitative coronary angiography measurements were analyzed, and their correlation with maximum CT values for the vessel short axes was determined. A rapid accurate method for such measurements was sought by substituting maximum CT values for the descending aorta in the corresponding axial images for those for the short axes.
Methods and Results In 8 patients, 179 sites were measured. Means (±SD) of adjusted thresholds and the maximum CT values for vessel short axes and the descending aorta in the corresponding axial images for all vessels were 108±66, 227±80, and 363±75 Hounsfield Unit (HU), respectively. Adjusted thresholds correlated with the maximum CT values for the corresponding vessel short axes and the descending aorta in the corresponding axial images, with R^2=0.55, 0.33, $p<0.01$, respectively. An abbreviated formula for use of maximum CT values for the descending aorta in the corresponding axial images was y=0.5x–75 (HU) (y=adjusted threshold, x=maximum CT value for the descending aorta in the corresponding axial image).
Conclusions The abbreviated formula provided a rapid, accurate method for measurements independent of arterial enhancement. (*Circ J* 2004; **68:** 769–777)

Key Words: Adjusted thresholds; Coronary artery; Electron beam computed tomography; Quantitative coronary angiography

Measurements of the diameters of 3-dimensional (3-D) coronary arteries using electron-beam computed tomography (EBCT) and shaded surface display (SSD) techniques have been qualitatively compared with those obtained by cine coronary angiography[1–3] The threshold selection has been set at 80–100 Hounsfield Units (HU) and from quantitative analysis using different threshold selections[4] it is reasonable to expect that the optimal threshold level for SSD depends on the magnitude of arterial enhancement. As a result, we hypothesized that a single threshold setting would not constitute a reliable measurement of coronary arterial luminal diameter using EBCT. We have previously reported that adjusted threshold methods using line density profile (LDP) curves in consideration of arterial enhancement provided more accurate results than fixed threshold methods[5,6] However, in routine practice it is unrealistic to make an LDP curve, or to measure the maximum computed tomography (CT) value for the short axis at each site in the coronary arteries.

In the present study, we analyzed the adjusted thresholds at which the diameters of coronary arteries determined by EBCT scans are equal to the corresponding quantitative coronary angiography (QCA) measurements. Calibration using aortic opacity of the opacified blood, and using maximum CT values for the descending aorta in the corresponding axial images as a substitute for the maximum CT values for the short axes of the coronary arteries, was performed to accurately resolve the measurements of coronary artery luminal diameter. Furthermore we sought to establish a simplified method for measuring coronary artery diameters that was independent of inter- and intra-patient variations in arterial enhancement.

Methods

Patients

Under a protocol approved by the institutional committee for the protection of human subjects and after informed consent was obtained, 8 male patients aged 53–63 years old, who had previously undergone heart transplantation at a mean 3.6 years prior to enrollment, were recruited to undergo both EBCT (Imatron C-150XP, Imatron, South San Francisco, CA, USA) and cine coronary angiography within a 24-h period.

(Received February 24, 2004; revised manuscript received May 13, 2004; accepted May 28, 2004)
*Department of Cardiovascular Science and Medicine, Chiba University Graduate School of Medicine, Chiba, *First Department of Internal Medicine, Osaka City University, Osaka, **GE Yokokawa Medical Systems, Tokyo and †Department of Radiology, Stanford University School of Medicine, California, USA*
Mailing address: Nobusada Funabashi, MD, Department of Cardiovascular Science and Medicine, Chiba University Graduate School of Medicine, 1-8-1 Inohana, Chuo-ku, Chiba, Chiba 260-8670, Japan. E-mail: nobusada@ma.kcom.ne.jp

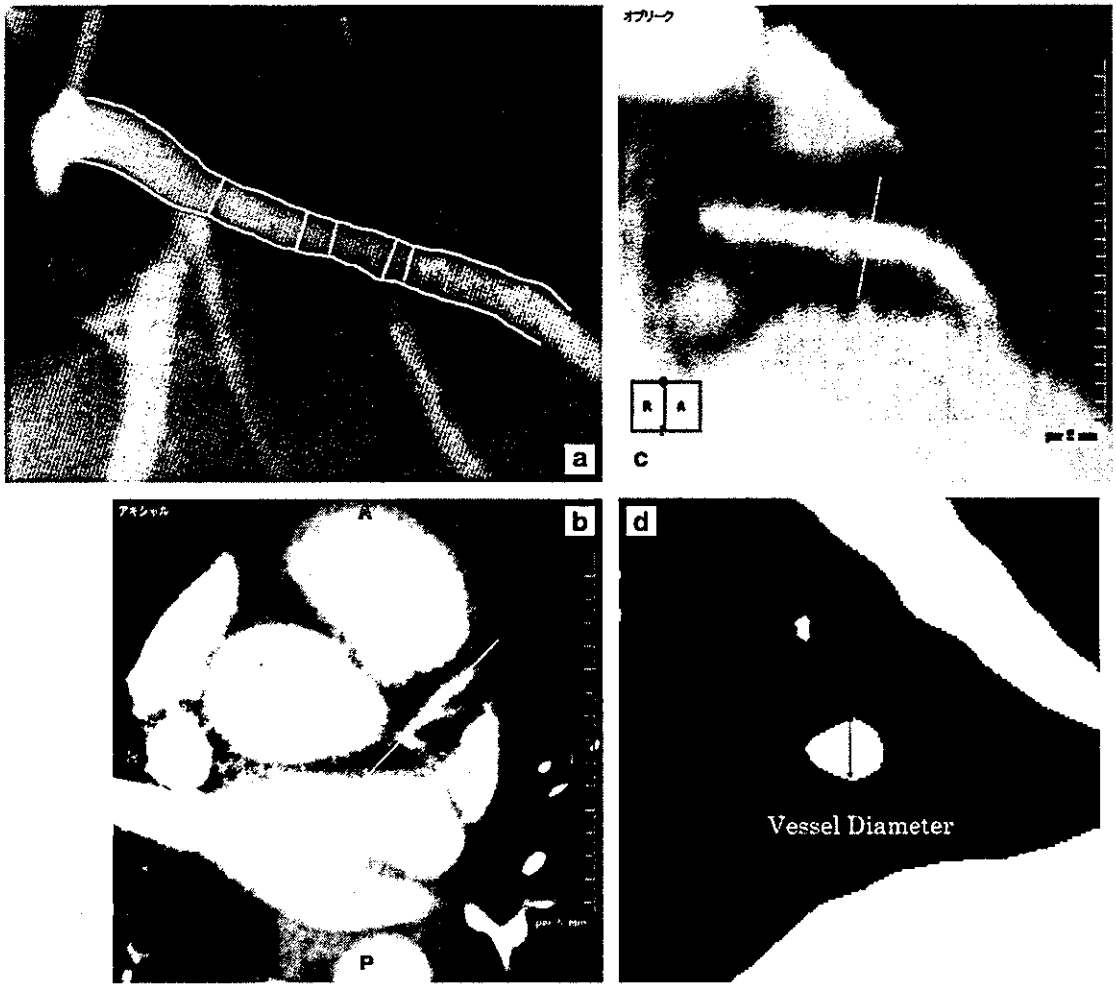

Fig 1. (a) Quantitative coronary angiogram showing the 30-degree right anterior oblique projection of the left coronary arteries. Lines indicate manual tracing. (b–d) Schema of measurement of adjusted thresholds using electron-beam computed tomography (CT). (b) Transverse source image obtained with contrast-enhanced electron-beam CT. The yellow line indicates the long axis of the LAD branch with which we measured vessel diameters. (c) Oblique planar image parallel to the long axis of the LAD branch. The yellow line indicates the axis perpendicular to the long axis of the vessel. Diameters were measured perpendicular to the median centerline of the vessel. Oblique planar reformations were generated parallel to the long axis of vessel, which approximates the oblique projections analyzed with cine coronary angiography. (d) Oblique planar image perpendicular to the long axis of the LAD branch. By setting the display width at zero, we were able to reduce the grayscale to black and white. We set the window levels at the site at which the vessel diameters were equal to the diameters measured by quantitative coronary angiography (QCA) measurement; these window levels were regarded as the adjusted thresholds. Vessel diameters were measured at each measurement site in the same direction as for the coronary angiograms.

Cine Coronary Angiography

Cine coronary angiography was performed using the percutaneous femoral approach. Sublingual nitroglycerin (0.4 mg) was given 2–3 min before the contrast injection, to minimize the effect of varying vasomotor tone on vessel lumen diameters. Catheters of known diameters were used for calibration. Multiple projections, including cranial and caudal angulated views, were obtained for all patients. The 30-degree right anterior oblique (RAO) projection was used to assess the left coronary artery (LCA) and its branches, and the 60-degree left anterior oblique (LAO) projection was used to assess the right coronary artery (RCA).

QCA was performed off-line using a computerized edge detection program (QCA plus, Sanders Data System, Palo Alto, CA, USA) developed and validated at Stanford[7] and analyzed by a cardiologist (Y.K.) unaware of the EBCT results (Fig 1a). Diameters of the proximal left main (LM) artery and its distal end just above the bifurcation of the left anterior descending branch (LAD) and the left circumflex branch (LCX) were recorded, as well as the diameter at a point between these 2 sites. Also measured were the diameters of the LAD, the LCX, and the RCA, each at their proximal ends and at 2–4 equally spaced points between their proximal ends and the first atrial side branch. Single end-diastolic cine frames, identified by an electrocardiogram-triggered mark on the frames and selected for optimal coronary vessel opacification, were focused and magnified. The digitized image was displayed on a graphic computer terminal linked to a light pen, which was used to manually trace the margins of either the catheter or coronary segment. Using these lines as initial search locations, the automatic edge-finding algorithm drew and smoothed the edges, defining the edge as the peak of the first derivative of the gray-scale density gradient, perpendicular to the long axis

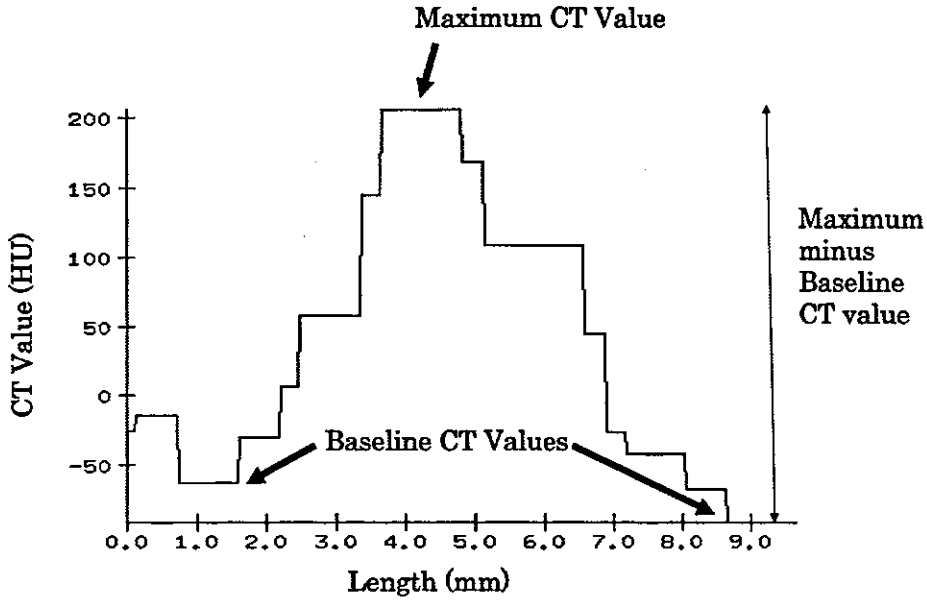

Fig 2. Schema of line density profile (LDP) method. Plot shows the voxel values along a line that is perpendicular to the median centerline of the vessel at each measurement site. In this schema, the baselines of the LDP were established as the epicardial fat immediately adjacent to the vessel on both sides. For the LDP curve, baseline computed tomography (CT) values were calculated for the right side and the left side in addition to the maximum CT value represented as the schema. We measured the maximum CT value minus baseline CT value at both sides and used both the larger and average values.

of the catheter or vessel, as estimated from the initial manual tracings. When the computer algorithm was unable to resolve vessel boundaries in areas of noise or vessel crossings, manual editing of short segments of boundary with the light pen was used to correct the computer-generated boundary. At no time did the length of a manually entered margin exceed 20% of the total length of the quantitated segment. After the light pen indicated the start and end of the segment, the mean diameter of the segment was computed from perpendiculars constructed through the length of a computer-generated centerline. The distance of each measurement point from the LM or the RCA ostium was measured.

EBCT Measurement

EBCT attains ultrafast scan speeds by sweeping a steered electron beam on a fixed tungsten target ring, thereby providing a moving X-ray source without mechanical motion[8] The 100-ms modes are used for high-resolution cross-section imaging in a Step-Volume Scan mode with electrocardiogram gating[9] EBCT was coupled to a 160 ml intravenous injection of iodinated contrast material (300 mg/ml) performed during breath holding, and was directed over 60–70 mm of the proximal and middle portions of the coronary arteries using 1.5 mm collimation, 1.0 mm table incrementation, and triggered to 80% of the R-to-R interval. The patients received nitroglycerin prior to EBCT, as in the cine angiography studies.

EBCT data were transferred to a workstation (Advantage-Windows, General Electronics, Milwaukee, WI, USA) and 18–27 measurement points per patient within the coronary tree were defined relative to identifiable branches.

Vessel diameters were measured at each measurement site in the same direction as the QCA measurements. Diameters were analyzed by a cardiologist (N.F.) unaware of the QCA results, using the workstation program described later (Fig 1 b–d). Double oblique planar reformations were generated, firstly parallel to the long axes of the vessels, approximating the oblique projections analyzed by cine coronary angiography (Fig 1 b,c). Using the vessel origins and the major branch sites as landmarks, the loci corresponding to the QCA measurement were identified on the EBCT scans. Second, an additional oblique planar reformation was generated perpendicular to the first oblique reformation image (long axes of the vessel) (Fig 1c). By setting the display width at zero, we were able to reduce the grayscale to black and white (Fig 1d). We set the window levels at the site at which vessel diameters were equal to the diameters obtained by QCA measurement; these window levels were regarded as the adjusted thresholds. Furthermore, LDP curves were made perpendicular to the median centerline of the vessel at each measurement site. A plot of the voxel values along a line perpendicular to the vessel at each measurement site was created (Fig 2). The baseline of the LDP was established as epicardial fat or myocardium immediately adjacent to the artery. For the LDP curve, baseline CT values were calculated for the right and left sides in addition to the maximum CT value. We measured the maximum CT value minus baseline CT value using the larger and average values for both sides in the scatter plot. The maximum CT value for the short axis of the coronary arterial lumen at each measurement site was measured from the oblique planar reformations perpendicular to the long axis of the vessel. Also, the maximum CT value for the descending aorta at the corresponding axial level of each measurement site was measured. As some calcifications, which apparently caused a higher attenuation than the vessel lumen, were evident on the enhanced axial images of the descending aorta, we carefully excluded them and measured the maximum CT values for the descending aorta. The maximum CT value was used as an index for assessing arterial enhancement.

Table 1 QCA Diameter With Distance From the Ostium

Vessel type	n	QCA Diameter (mm)	Distance from Ostium (mm)
LM	11	5.07±0.75 (3.82–6.09)	3.21±2.9 (0–9.39)
LAD	62	3.3±0.85 (1.46–5.28)	34.64±17.13 (5–77.64)
LCX	46	3.53±0.76 (1.52–5.27)	23.81±15.16 (3–62.54)
RCA	60	3.61±0.58 (2.71–5.67)	28.56±20.93 (0–79.77)
Total	179	3.57±0.84 (1.46–6.09)	27.89±19.04 (0–79.77)

QCA, quantitative coronary arterigraphy; LM, left main; LAD, left anterior descending branch; LCX, left circumflex branch; RCA, right coronary artery.

Table 2 QCA Diameter, Distance From the Ositum, Adjusted Threshold, and Maximum CT Values for Each Patient

Patient no.	n	QCA Diameter (mm)	Distance from ostium (mm)	Adjusted threshold (HU)	Maximum CT value in short axis (HU)	Maximum CT value in aorta (HU)
1	18	3.31±1.19	22.2±16.3	138±44	214±37	344±28
2	23	3.25±0.73	25.9±17.4	80±35	169±57	293±22
3	20	4.06±0.9	20.1±17.6	148±32	282±33	376±31
4	20	3.57±0.46	25.2±16.6	85±46	210±37	374±14
5	26	3.57±0.69	30.2±16.9	196±41	327±92	475±40
6	24	3.57±0.56	32.5±21.4	69±39	243±65	412±25
7	21	3.57±0.48	26.1±15.7	110±59	213±56	349±27
8	27	3.57±0.64	36.2±21.8	48±59	155±43	276±76
Total	179	3.57±0.84	27.9±19	108±66	227±80	363±75

QCA, quantutative coronary arteriography; HU, Hounsfield Units.

Table 3 QCA Diameter, Distance From the Ostium, Adjusted Threshold, and Maximum CT Values for Each Vessel

Vessel site	n	QCA diameter (mm)	Distance from ostium (mm)	Adjusted threshold (HU)	Maximum CT value in short axis (HU)	Maximum CT value in aorta (HU)
LM	11	5.07±0.72	3.2±2.8	112±42	263±71	349±49
LAD	62	3.3±0.84	34.6±17	107±69	207±71	338±82
<30 mm from ostium	25	3.88±0.74	18.7±7.4	79±64	204±71	337±78
≥30 mm from ostium	37	2.92±0.67	45.4±12.6	127±65	209±72	339±86
LCX	46	3.53±0.75	23.8±15	85±55	203±52	368±63
<30 mm from ostium	30	3.66±0.74	14.3±6.5	80±49	208±46	355±62
≥30 mm from ostium	16	3.29±0.72	41.6±9	94±63	192±61	393±58
RCA	60	3.61±0.57	28.6±20.8	126±70	259±93	387±69
<30 mm from ostium	31	3.81±0.61	11.6±9.3	118±78	256±93	371±67
≥30 mm from ostium	29	3.4±0.44	46.7±12.7	135±59	262±92	404±68
Total	179	3.57±0.84	27.9±19	108±66	227±80	363±75

QCA, quantitative coronary arteriography; LM, left main; LAD, left anterior descending branch; LCX, left circumflex branch; RCA, right coronary artery; HU, Hounsfield Units.

Statistical Analysis

Adjusted thresholds were correlated with arterial enhancement (maximum CT values for the vessel short axes, the descending aorta in the corresponding axial images, vessel sizes (the corresponding QCA diameter measurements), and the distances from the vessel ostium. Variations between the 2 groups (adjusted thresholds and thresholds according to the abbreviated formula) were compared using the F distribution test.

Results

QCA Diameters With Distances From the Ostium

All 8 cine coronary angiograms were interpreted as being normal. A total of 179 sites were measured among the 8 patients (LM, 11; LAD, 62; LCX, 46; RCA, 60).

Table 1 lists the QCA diameters with the distances from the LM or RCA ostium. The QCA diameters ranged from 1.46 mm to 6.09 mm (mean ± SD, 3.57±0.84 mm). Distances from the ostium ranged from 0 to 79.77 mm (27.9± 19.04 mm).

EBCT Measurement With Arterial Enhancement

Table 2 lists the number of vessel sites, QCA diameters (mean ± SD), distances from the ostium, adjusted thresholds, and maximum CT values for the vessel short axes and the descending aorta in the corresponding axial images for each patient.

Table 3 lists the number of vessel sites, distances from the ostium (mean ± SD), adjusted thresholds and maximum CT values for the vessel short axes and the descending aorta in the corresponding axial images for each vessel type. Values were further stratified according to the position of measurement from the vessel ostium. Adjusted thresholds, maximum CT values for vessel short axes and maximum CT values for the descending aorta in the corresponding axial images for all vessels were 108±66, 227± 80, and 363±75 HU, respectively.

All sites corresponding to the maximum CT values for both the vessel short axes and the descending aorta in the corresponding axial images were located approximately at the center of the vessel lumen. After review of the cine coronary angiograms and the enhanced axial images of the

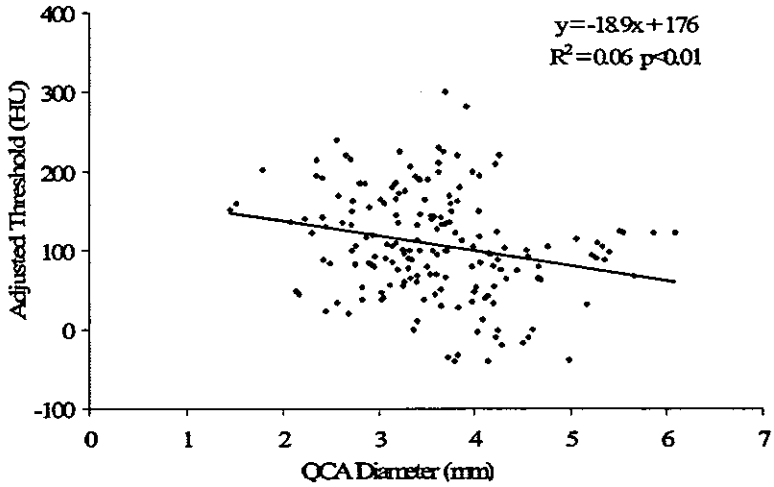

Fig 3. Scatter plot of adjusted threshold vs quantitative coronary angiography (QCA) diameter. The adjusted thresholds very weakly correlated with the QCA diameters (R^2=0.06, p<0.01). These mean values were distributed about a straight line given by y=18.9x−176.

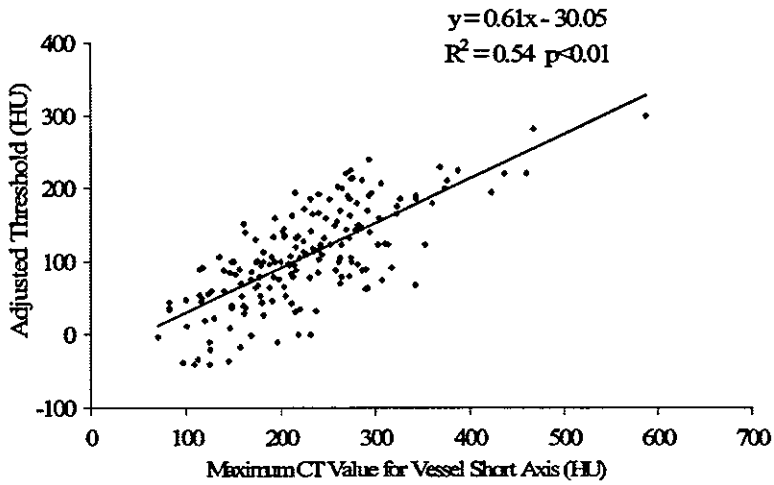

Fig 4. Scatter plot of adjusted threshold vs maximum computed tomography (CT) value for the corresponding vessel short axis. The adjusted thresholds correlated with the maximum CT values for the corresponding vessel short axes (R^2=0.54, p<0.01).

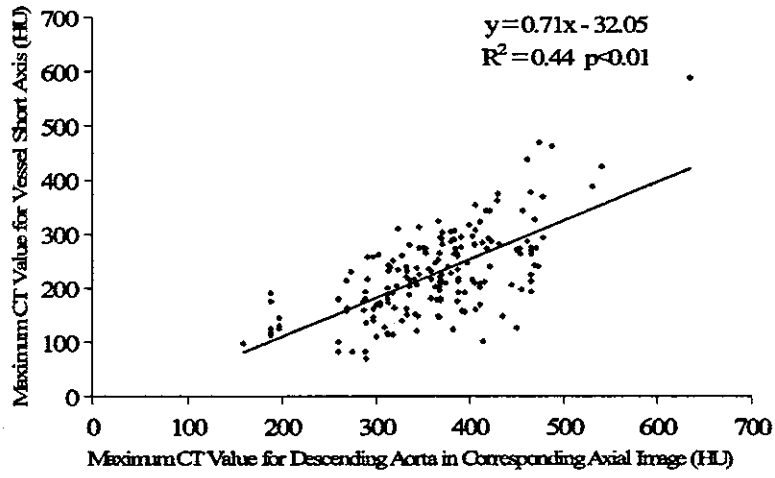

Fig 5. Scatter plot of maximum computed tomography (CT) value for the vessel short axis with maximum CT value for the descending aorta in the corresponding axial image. The maximum CT values for the vessel short axes correlated with those for the descending aorta in the corresponding axial images (R^2=0.44, p<0.01). These mean values were distributed about a straight line given by y=0.71x−32.1.

EBCT data sets, we concluded that the possibility of the presence of calcification or artifact in the coronary arteries might be low; nevertheless, we were careful not to adopt the CT values relating to calcification when calculating maximum CT values for the descending aorta.

As shown in Fig 3, the adjusted thresholds correlated very weakly with QCA diameters, with R^2=0.06, p<0.01. These mean values were distributed about a straight line given by y=−18.9x+176.

The adjusted thresholds correlated with maximum CT values for the corresponding vessel short axes, with R^2= 0.54, p<0.01 (Fig 4). These mean values were distributed about a straight line given by y=0.61x−30.1. As shown in Fig 5, the maximum CT values for the vessel short axes correlated with those for the descending aorta in the corresponding axial images with R^2=0.44, p<0.01. These mean

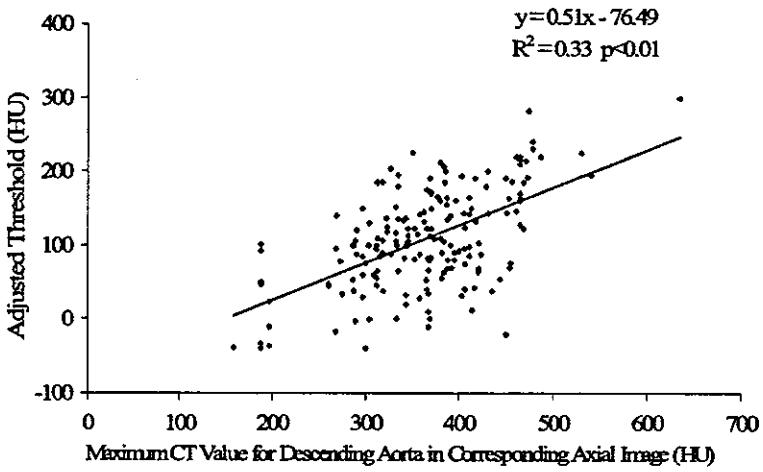

Fig 6. Scatter plot of adjusted threshold with maximum computed tomography (CT) value for the descending aorta in the corresponding axial image. The adjusted thresholds correlated with the maximum CT values for the descending aorta in the corresponding axial images (R^2=0.33, p<0.01). These mean values were distributed about a straight line given by y=0.51x−76.5. The slope of the adjusted thresholds vs the maximum CT values for the descending aorta in the corresponding axial images was approximately 0.5. The intercept of this line was −76.5 HU.

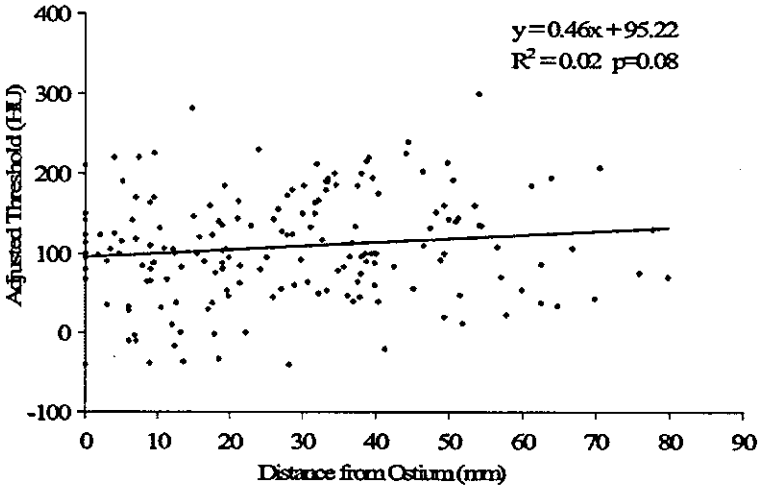

Fig 7. Scatter plot of adjusted threshold vs distance from the ostium. The adjusted thresholds did not correlate significantly with distances from the ostium (R^2=0.02, p=0.08).

values were distributed about a straight line given by y=0.71x−32.1.

The adjusted thresholds correlated with the maximum CT values for the descending aorta in the corresponding axial images with R^2=0.33, p<0.01 (Fig 6). These mean values were distributed about a straight line given by y=0.51x−76.5. The slope of the adjusted thresholds vs the maximum CT values for the descending aorta in the corresponding axial images was approximately 0.5. The intercept of this line was −76.5 HU.

As shown in Fig 7, the thresholds did not correlate significantly with distances from the ostium, with R^2=0.02, p=0.08.

As shown in Fig 8a, the adjusted thresholds correlated with the maximum minus the baseline CT values in the LDP (average of the 2 sides), with R^2=0.30, p<0.01. These mean values were distributed about a straight line given by y=0.43x−15.8. As shown in Fig 8b, the adjusted thresholds correlated with the maximum minus the baseline CT values in the LDP (larger of the 2 sides), with R^2=0.37, p<0.01. These mean values were distributed about a straight line given by y=0.47x−40.4.

From the straight line given by y=0.51x−76.5 in Fig 6, (y=adjusted threshold, x=maximum CT value for the descending aorta in the corresponding axial images), we determined the thresholds according to the abbreviated formula whereby y=0.5x−75 (HU) (y=adjusted threshold, x=maximum CT value for the descending aorta in the corresponding axial image). The constant, −75 HU, may reflect a complex of various baseline (or background) factors such as epicardial fat or myocardium. The mean (±SD) baseline CT values of the LDP of the total, the group considered to be epicardial fat and the group considered to be myocardium, were −61.0±60.4, −82.5±38.6, and 41.6±35.3 HU with ranges of −181 to 150, −181 to −2, and 0 to 150 HU, respectively.

As shown in Fig 9, the adjusted thresholds correlated with the thresholds determined by the abbreviated formula, with R^2=0.33 p<0.01. These mean values were distributed about a straight line given by y=1.02x−0.4. The slope of the adjusted thresholds vs the thresholds according to the abbreviated formula was approximately 1.0, and the intercept of this line was only −0.4 HU. In addition, the mean± SD of thresholds by the abbreviated formula was 107± 37 HU. In comparing the mean±SD of the adjusted thresholds, the mean of the thresholds by the abbreviated formula was similar (107 vs 108 HU), but the standard deviation was significantly smaller (37 vs 66 HU).

As shown in Fig 10, the CT angiography diameter correlated with QCA diameter (R^2=0.09 p<0.01). The mean values were distributed about a straight line given by y=0.50x+1.86.

Discussion

Cine coronary angiography has been the standard for

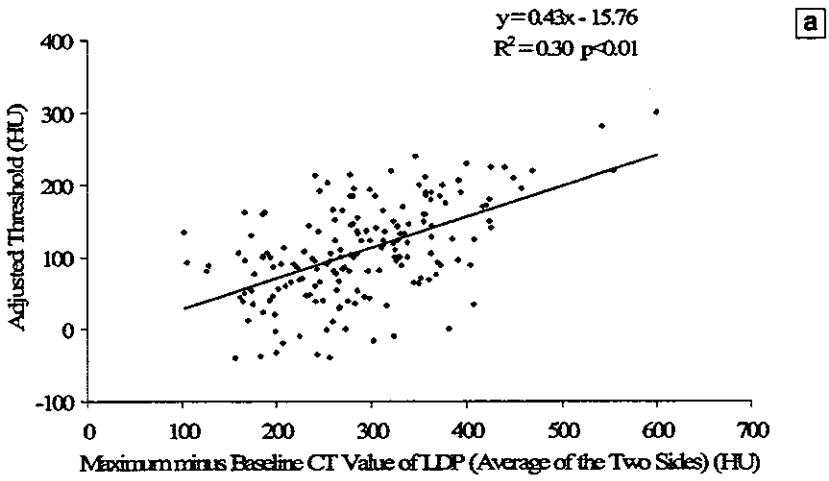

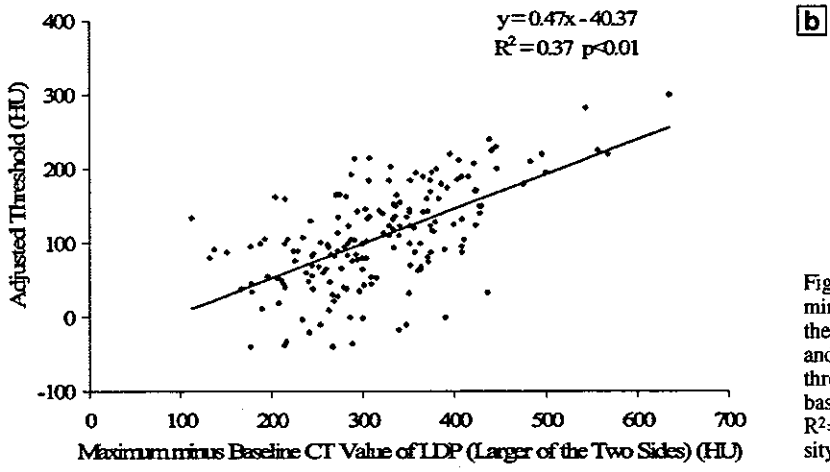

Fig 8. Scatter plots of adjusted threshold vs maximum minus the baseline computed tomography (CT) value in the line density profile (LDP) ((a) average of the 2 sides) and ((b) larger of the 2 sides). In (a) and (b), the adjusted thresholds were correlated with the maximum minus baseline CT values in the LDP (R^2=0.30, p<0.01 and R^2=0.37, p<0.01, respectively). LDP indicates line density profile.

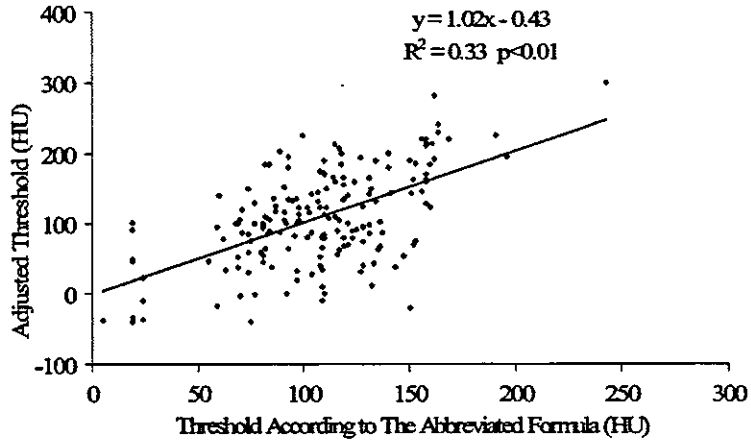

Fig 9. Scatter plot of adjusted threshold vs threshold obtained by an abbreviated formula. The adjusted thresholds correlated with threshold according to the formula (R^2=0.33, p<0.01). The mean values were distributed about a straight line given by y=1.02x–0.4. The slope of the line was approximately 1.0 and the intercept was –0.4 HU.

evaluating the extent of coronary artery disease, but recently 3-D visualization of coronary arteries using EBCT has emerged as a potential non-invasive alternative[1,2,10] Although qualitative reports have been published regarding the utility of EBCT coronary angiography[1,11–13] there are few reports of quantitative analysis of EBCT coronary angiography as compared with cine coronary angiography[5,6] We have speculated that several factors may influence the absolute luminal caliber of coronary arteries on EBCT angiograms, such as arterial enhancement, vessel diameter, distance from the ostium, and vessel types triggered to contract at the end of diastole[6]

Because the acquisition time requires 40–80 heartbeats, there must be significant differences in the state of the enhancement at the level of each slice[14] We first made a short-axis image of the coronary arteries at each site and measured the adjusted threshold at which vessel diameter was equal to that obtained from the corresponding QCA measurement.

Even though the total mean of the adjusted threshold was 108 HU, we concluded that a single threshold setting could not be used reliably to measure the luminal diameter

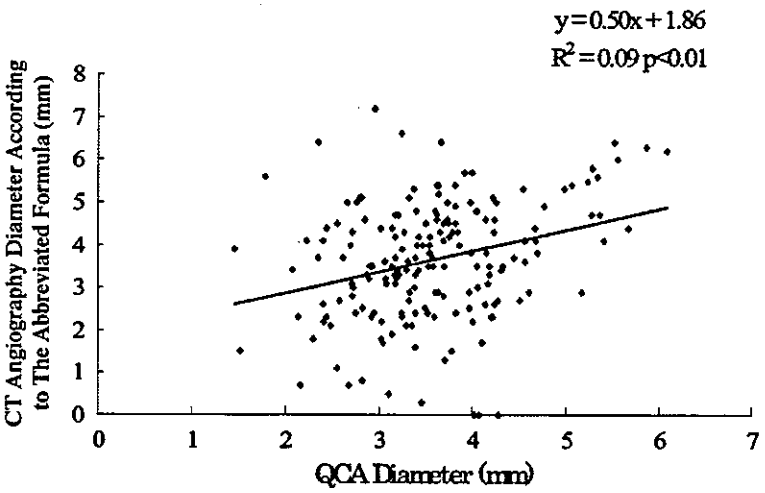

Fig 10. Scatter plot of computed tomography (CT) angiography diameter according to the abbreviated formula (mm) vs quantitative coronary angiography (QCA) diameter (mm). The CT angiography diameter according to the abbreviated formula (mm) correlated with QCA diameter (R^2=0.09 $p<0.01$). The mean values were distributed about a straight line given by y=0.50x+1.86.

of the coronary arterial tree with EBCT. However, it is unrealistic to make an LDP curve or measure the maximum CT value for the short axis at each site of the coronary arteries in routine practice. Therefore, another, easier method was needed. For this, we focused on the maximum CT values for the descending aorta in the corresponding axial images. In theory, it would be better to use the maximum minus baseline CT values than the maximum CT values alone. Therefore, we also considered the correlation between the values of R^2=0.30 for the average of the 2 sides and 0.37 for the larger of the 2 sides. Those values adjusted the thresholds with the maximum minus baseline CT values in the LDP, which gave less than the maximum CT values alone for the short axes.

To use the maximum CT values for the descending aorta in the corresponding axial images, we applied the abbreviated formula y=0.5x−75 from the straight line given by y=0.51x−76.5 (y=adjusted threshold, x=maximum CT value for the descending aorta in the corresponding axial image). If our abbreviated formula, y=0.5x−75, is to be adopted, it is necessary to measure the maximum CT values for the descending aorta in the corresponding axial images. By including the maximum intensity projection technique, it may be easy to measure the maximum CT values for the descending aorta at each axial image level and acquire information about arterial enhancement for every slice.

The adjusted thresholds correlated with the thresholds obtained from the abbreviated formula, with R^2=0.33, and the mean values were distributed about a straight line given by y=1.02x−0.4. The slope of the adjusted thresholds vs the thresholds according to the abbreviated formula was approximately 1.0, and the intercept of this line was only −0.4 HU. In comparing the thresholds according to the abbreviated formula with the adjusted thresholds, the means were similar but the standard deviation was significantly smaller in the thresholds obtained from the abbreviated formula. Therefore, adoption of the thresholds by the abbreviated formula makes it possible to achieve accurate measurements for the evaluation of coronary arteries.

In the scatter plot of the adjusted threshold vs the QCA diameter (Fig 3), the smaller the vessel diameter, the greater the adjusted threshold. Achenbach et al reported that when using 100 HU as the fixed lower threshold, they tended to underestimate small vessel diameters by the partial volume effect[15] We obtained the opposite result and we speculate that this phenomenon might also be caused by other factors such as vessel type, arterial enhancement, vessel orientation, etc. For example, as shown in Table 3, the mean of the adjusted threshold for the portions of the RCA that were 30 mm or more from the ostium was 135 HU, whereas that of the portions of LCX at 30 mm or more from the ostium was 94 HU. Thus, when we adopted 100 HU as the fixed lower threshold, we overestimated the diameters of the portion of RCA that were 30 mm or more from the ostium, but underestimated those of the portion of the LCX that were 30 mm or more from the ostium. The adjusted thresholds correlated very weakly, or non-significantly, to the corresponding diameters measured by QCA, or the distances from the ostium, respectively.

Recently, 16-detector row multislice computed tomography (MSCT)[16,17] has become available and takes less than 25 s to image the whole heart, even if a slice thickness less than 1 mm is selected; this time interval is approximately half to one-third that required for EBCT. Therefore with MSCT, differences in the degree of arterial enhancement would influence the quality of the coronary arterial images to a lesser extent than with EBCT. Some investigators have tried to keep the same degree of arterial enhancement by improving the method of injection of the contrast material, for example via the biphase injection protocol[18] If the MSCT coronary angiogram replaced the conventional coronary angiogram only for evaluation of the coronary arterial lumen, the calibration with aortic opacity of the opacified blood would improve the quantitative accuracy of the vessel diameters. Further studies using up-to-date MSCT and EBCT are needed to quantitatively compare the coronary artery diameters with those from QCA.

Although EBCT has worse spatial resolution than MSCT, especially in the through-plane, EBCT delivers a much lower radiation dose than MSCT, so it is still an important diagnostic modality, especially for healthy subjects.

Conclusion

We measured the adjusted thresholds at which the coronary arterial diameters on EBCT scans were equal to those obtained by a QCA measurement program. We classified a total of 179 sites among 8 patients and 4 vessel types, and further stratified measurements according to positions in relation to the vessel ostium. The means of the adjusted thresholds changed from patient to patient and from vessel

to vessel.

The adjusted thresholds correlated only very weakly, or non-significantly, with the corresponding QCA measurement diameters, or with the distances from the ostium. However, there was a correlation with maximum CT values for the vessel short axes. Therefore, we decided to use the maximum CT value for the vessel short axis as an index for assessing arterial enhancement. However, it is unrealistic in routine practice to make an LDP curve, or to measure the maximum CT value for the short axis at each site in the coronary artery. Therefore, using the maximum CT values for the descending aorta in the corresponding axial images as a substitute for the maximum CT values for the short axes of coronary arteries, and the abbreviated formula, y=0.5x–75, we developed an accurate and straightforward method for measuring the diameters of coronary arteries independent of arterial enhancement.

Acknowledgments

This work was supported by the Japan Cardiovascular Research Foundation, Takeda Science Foundation and GE Yokokawa Medical Systems.

References

1. Moshage WEL, Achenbach S, Seese B, Bachmann K, Kirchgeorg M. Coronary artery stenosis: Three-dimensional imaging with electrocardiographically triggered, contrast agent-enhanced, electron-beam CT. *Radiology* 1995; **196:** 707–714.
2. Achenbach S, Moshage W, Ropers D, Nossen J, Daniel WG. Value of electron-beam computed tomography for the noninvasive detection of high-grade coronary-artery stenoses and occlusions. *N Engl J Med* 1999; **339:** 1964–1971.
3. Budoff MJ, Oudiz RJ, Zalace CP, Bakhsheshi H, Goldberg SL, French WJ, et al. Intravenous three-dimensional coronary angiography using contrast enhanced electron beam computed tomography. *Am J Cardiol* 1999; **83:** 840–845.
4. Shimamoto R, Suzuki J, Nishikawa J, Fujimori Y, Nakamura F, Shin WS, et al. Measuring the diameter of coronary arteries on MR angiograms using spatial profile curves. *AJR Am J Roentgenol* 1998; **170:** 889–893.
5. Funabashi N, Rubin GD, Kobayashi Y, Shifrin RY, Wexler L, Perlroth M. Accuracy of coronary artery dimensions with electron-beam CT angiography: Comparison of measurement methods (abstract). *Radiology* 1999; **213(P):** 269.
6. Funabashi N, Kobayashi Y, Perlroth M, Rubin GD. Coronary artery; quantitative evaluation of normal artery diameter measurements determined by electron-beam computed tomography in comparison with cine coronary angiography: Initial experience. *Radiology* 2003; **226:** 263–271.
7. Pomerantsev EV, Kobayashi Y, Fitzgerald PJ, Grube E, Sanders WJ, Alderman EL, et al. Coronary stents: In vitro aspects of an angiographic and ultrasound quantification with in vivo correlation. *Circulation* 1998; **98:** 1495–1503.
8. Gould RG. Principles of ultrafast computed tomography: Historical aspects, mechanism of action, and scanner characteristics. *In*: Stanford W, Rumberger J, editors. Ultrafast computed tomography in cardiac imaging: Principles and practice. New York: Futura; 1992; 1–15.
9. Rumberger JA. Ultrafast computed tomography scanning modes, scanning planes and practical aspects of contrast administration. *In*: Stanford W, Rumberger J, editors. Ultrafast computed tomography in cardiac imaging: Principles and practice. New York: Futura; 1992; 17–24.
10. Chernoff DM, Ritchie CJ, Higgins CB. Evaluation of electron beam CT coronary angiography in healthy subjects. *AJR Am J Roentgenol* 1997; **169:** 93–99.
11. Funabashi N, Misumi K, Ohnishi H, Watanabe M, Suzuki Y, Imai N, et al. Endoluminal perspective volume rendering of coronary arteries using electron-beam computed tomography. *Circ J* 2003; **67:** 1064–1067.
12. Funabashi N, Matsumoto A, Yoshida T, Watanabe S, Misumi K, Masuda Y. Usefulness of three-dimensional visualization of coronary arteries using electron-beam computed tomography data with volume rendering. *Jpn Circ J* 2000; **64:** 644–646.
13. Funabashi N, Kobayashi Y, Rubin GD. Utility of three-dimensional volume rendering images using electron-beam computed tomography to evaluate possible causes of ischemia from an anomalous origin of the right coronary artery from the left sinus of Valsalva. *Jpn Circ J* 2001; **65:** 575–578.
14. Nakanishi T, Kohata M, Miyasaka K, Fukuoka H, Ito K, Imazu M. Virtual endoscopy of coronary arteries using contrast-enhanced ECG-triggered electron beam CT data sets. *AJR Am J Roentgenol* 2000; **174:** 1345–1347.
15. Achenbach S, Moshage W, Ropers D, Bachmann K. Comparison of vessel diameters in electron beam computed tomography and quantitative coronary angiography. *Int J Card Imaging* 1998; **14:** 1–7.
16. Ropers D, Baum U, Pohle K, Anders K, Ulzheimer S, Ohnesorge B, et al. Detection of coronary artery stenoses with thin-slice multi-detector row spiral computed tomography and multiplanar reconstruction. *Circulation* 2003; **107:** 664–666.
17. Sato Y, Kanmatsuse K, Inoue F, Horie T, Kato M, Kusama J, et al. Noninvasive coronary artery imaging by multislice spiral computed tomography. *Circ J* 2003; **67:** 107–111.
18. Fleischmann D, Rubin GD, Bankier AA, Hittmair K. Improved uniformity of aortic enhancement with customized contrast medium injection protocols at CT angiography. *Radiology* 2000; **214:** 363–371.

Case Report

Steroid-responsive thromboangiitis obliterans

Lancet 2004; 364: 1098

Atsuhiko T Naito, Tohru Minamino, Kaoru Tateno, Toshio Nagai, Issei Komuro

Department of Cardiovascular Science and Medicine (A T Naito MD, T Minamino MD, K Tateno MD, T Nagai MD, I Komuro MD) Chiba University Graduate School of Medicine, 1-8-1 Inohana, Chuo-ku, Chiba 260-8670, Japan

Correspondence to: Dr Issei Komuro komuro-tky@umin.ac.jp

A 41-year-old, non-smoking man came to the emergency room in June, 2003, complaining of cold, painful hands. On examination, we found nothing abnormal, apart from cyanotic, tender fingers, with poor perfusion as shown on by laser doppler and infrared thermography (figure). Blood tests showed eosinophilia; 3097/μL, and eosinophilic cationic protein (ECP), >150 μg/mL (normal <14·7 μg/mL). Acute-phase reactants, C-reactive protein and the erythrocyte sedimentation rate were within normal limits. Chest radiographs and echocardiography showed no abnormalities or evidence of eosinophilia-induced end-organ damage. Angiography showed occlusion of the distal arteries of upper and lower extremities. We searched for parasitic infections and malignancy, to no avail. We excluded vasculitis from our differential diagnosis when the results of immunological tests showed no antinuclear, anticentromere, anticardiolipin, anti-dsDNA, anti-Scl70, anti-SS-A, anti-RNP, and anti-Jo1 antibodies, rheumatoid factor, ANCA, or cryoglobulins. Serum tryptase level was low; 3·9 ng/mL, indicating no involvement of mast cells. Our patient thus fulfilled the Japanese criteria for thromboangiitis obliterans,[1,2] and we started treatment with intravenous heparin and alprostadil. The patient's digital ischaemia and intermittent claudication showed no improvement after 1 week and his middle finger became necrotic. At that point, his eosinophil count was 5014/μL. We decided to give him prednisolone 30 mg daily, to treat the eosinophilia, in case it was contributing to the distal arterial occlusion. After 2 weeks of treatment, his eosinophil count and serum ECP levels decreased to 185/mm³ and 19·5 μg/mL, respectively. Laser doppler and infrared thermography showed a clear improvement in digital ischaemia (figure). When last seen in April, 2004, his fingers were completely healed, and he had no complaints of claudication.

A 62-year-old non-smoking man had been diagnosed with thromboangiitis obliterans in October, 1997, on the basis of angiography that showed occlusion of distal arteries in the absence of atherosclerosis. For 6 years, he had been treated with beraprost, anti-coagulants, lumbar sympathetic block, and continuous epidural block, but digital necrosis and pain persisted. He was admitted to our hospital in September, 2003. Blood tests showed eosinophilia; 2300/μL and ECP; 107 μg/mL. Tests for other causes of vascuolopathy were negative. We treated him with prednisolone, 30 mg daily, and after 2 weeks, his eosinophil count was 185/mm³ and serum ECP was 25·8 μg/mL. His pain had disappeared and his digital ischaemia largely resolved by the time of discharge in December, 2003.

Both of these patients fulfilled the Japanese criteria for thromboangiitis obliterans, but they were atypical patients because they were non-smokers at the onset of the symptoms. Current history of smoking is included in many case definitions of thromboangiitis obliterans.[1] Stopping smoking is the only proven strategy to prevent the progression of this disease, but 6-8% of Japanese patients diagnosed with thromboangiitis obliterans are non-smokers.[2] Hypereosinophilia causes end-organ damage by inducing thrombosis and endothelial damage, and simultaneous presentations of thromboangiitis obliterans with eosinophilia due to temporal arteritis have been reported.[3-5] However, we could find no reports of distal artery occlusion consistent with thromboangiitis obliterans and eosinophilia that responded to steroids. It will be interesting to see if patients who are diagnosed with thromboangiitis obliterans include a subset that have steroid-responsive disease, mediated by eosinophilia.

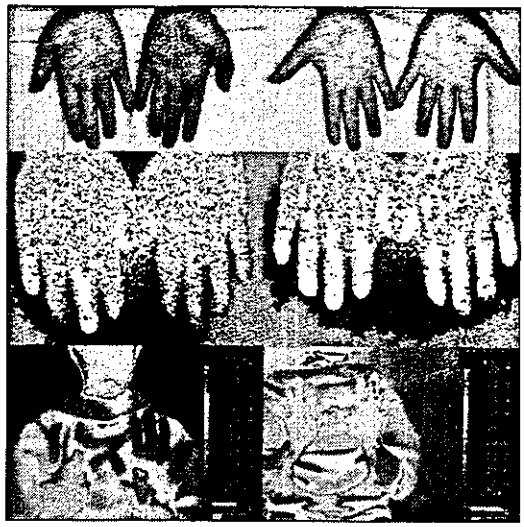

Figure: Photograph (top), laser doppler (middle), and infrared thermography (bottom), showing digital ischaemia before (left) and after steroid therapy (right).

References

1 Olin JW. Thromboangiitis obliterans (Buerger's disease). *N Engl J Med* 2000; 343: 864–69.

2 Sasaki S, Sakuma M, Yasuda K. Current status of thromboangiitis obliterans (Buerger's disease) in Japan. *Int J Cardiol* 2000; 75: S175–81.

3 Lie JT, Michet CJ Jr. Thromboangiitis obliterans with eosinophilia (Buerger's disease) of temporal arteries. *Hum Pathol* 1988; 19: 598–602.

4 Fujimoto M, Sato S, Hayashi N, Wakugawa M, Tsuchida T, Tamaki K. Juvenile temporal arteritis with eosinophilia: a distinct clinicopathological entity. *Dermatology* 1996; 192: 32–35.

5 Ferguson GT, Starkebaum G. Thromboangiitis obliterans associated with idiopathic hypereosinophilia. *Arch Intern Med* 1985; 145: 1726–28.

Vasorin, a transforming growth factor β-binding protein expressed in vascular smooth muscle cells, modulates the arterial response to injury *in vivo*

Yuichi Ikeda*†‡, Yasushi Imai†, Hidetoshi Kumagai*§, Tetsuya Nosaka*, Yoshihiro Morikawa¶, Tomoko Hisaoka¶, Ichiro Manabe†, Koji Maemura†, Takashi Nakaoka‖, Takeshi Imamura**, Kohei Miyazono††, Issei Komuro‡‡, Ryozo Nagai†, and Toshio Kitamura*‡§§

Divisions of *Hematopoietic Factors and §§Cellular Therapy and ‖Department of Advanced Medicine, Institute of Medical Science, University of Tokyo, Tokyo 108-8639, Japan; Departments of †Cardiovascular Medicine and ††Molecular Pathology, Graduate School of Medicine, University of Tokyo, Tokyo 113-8655, Japan; §Takada Research Laboratories, Chugai Pharmaceutical Company, Limited, Tokyo 171-8545, Japan; ¶Department of Anatomy and Neurobiology, Wakayama Medical School, Wakayama 641-8509, Japan; **Department of Biochemistry, Cancer Institute of the Japanese Foundation for Cancer Research, Tokyo 170-8455, Japan; and ‡‡Department of Cardiovascular Science and Medicine, Graduate School of Medicine, Chiba University, Chiba 260-8670, Japan

Communicated by Masashi Yanagisawa, University of Texas Southwestern Medical Center, Dallas, TX, June 9, 2004 (received for review February 25, 2004)

Growth factors, cell-surface receptors, adhesion molecules, and extracellular matrix proteins play critical roles in vascular pathophysiology by affecting growth, migration, differentiation, and survival of vascular cells. In a search for secreted and cell-surface molecules expressed in the cardiovascular system, by using a retrovirus-mediated signal sequence trap method, we isolated a cell-surface protein named vasorin. Vasorin is a typical type I membrane protein, containing tandem arrays of a characteristic leucine-rich repeat motif, an epidermal growth factor-like motif, and a fibronectin type III-like motif at the extracellular domain. Expression analyses demonstrated that vasorin is predominantly expressed in vascular smooth muscle cells, and that its expression is developmentally regulated. To clarify biological functions of vasorin, we searched for its binding partners and found that vasorin directly binds to transforming growth factor (TGF)-β and attenuates TGF-β signaling *in vitro*. Vasorin expression was down-regulated during vessel repair after arterial injury, and reversal of vasorin down-regulation, by using adenovirus-mediated *in vivo* gene transfer, significantly diminished injury-induced vascular lesion formation, at least in part, by inhibiting TGF-β signaling *in vivo*. These results suggest that down-regulation of vasorin expression contributes to neointimal formation after vascular injury and that vasorin modulates cellular responses to pathological stimuli in the vessel wall. Thus, vasorin is a potential therapeutic target for vascular fibroproliferative disorders.

Vascular smooth muscle cells (VSMCs), the major cell type in the vessel wall, show a spectrum of phenotypes, depending on environmental cues. Various injurious stimuli provoke the proliferation of differentiated medial VSMCs, which migrate to the intima and produce extracellular matrix proteins, resulting in the narrowing of the vascular lumen. These processes, called VSMC phenotypic modulation, play a key role in development of atherosclerotic diseases, such as postangioplasty restenosis, vein graft disease, and transplant vasculopathy. Whereas tremendous progress has been made in identifying growth factors and transcription factors that regulate the vascular response to injury, much information is lacking regarding cell-surface molecules that are involved in the pathogenesis of vascular fibroproliferative disorders. The signal sequence trap (SST) is a strategy to identify cDNAs containing signal sequence that encode secreted and type I membrane proteins (1, 2). We recently developed a refined SST system based on retrovirus-mediated expression screening (SST-REX) (3). In a search for secreted and cell-surface molecules expressed in the cardiovascular system, by using SST-REX, we identified a TGF-β binding protein, vasorin. Vasorin is predominantly expressed in VSMCs and modulates the vascular response to injury, at least in part, by attenuating TGF-β signaling *in vivo*. Here, we describe the molecular and functional characteristics of vasorin.

Methods

Cells and Reagents. A murine pro-B cell line Ba/F3 was maintained in RPMI medium 1640 containing 10% FCS and 2 ng/ml murine IL-3 (R & D Systems). Chinese hamster ovary (CHO) cells were grown in DMEM supplemented with 5% FCS and 1% nonessential amino acids (Invitrogen). Stable transfectants were established by the retrovirus expression system, by using a bicistronic retroviral vector pMX-IRES-EGFP as reported (4). Rat aortic VSMCs, prepared from 8-week-old Wistar rats by using the explant method (5), were grown in DMEM supplemented with 10% FCS. Primary antibodies used in this study were anti-Flag monoclonal antibody (M2, Sigma), anti-Smad2/3 monoclonal antibody (BD Transduction Laboratories), anti-phospho-Smad2 polyclonal antibody (Upstate, Charlottesville, VA), and anti-rat CD45 monoclonal antibody (BD Pharmingen).

Screening of a Human Heart cDNA Library by SST-REX and Cloning of the Full-Length cDNA Encoding *Vasorin*. A human heart cDNA library was screened by SST-REX as described (3). Briefly, cDNA was synthesized from poly(A)$^+$ RNA of human hearts (Clontech), by using the SuperScript Choice system (Invitrogen). The synthesized cDNA was separated based on size, and fractions >600 bp were inserted into *Bst*XI sites of the pMX-SST vector, by using *Bst*XI adapters (Invitrogen). Ba/F3 cells were infected with high-titer retroviruses expressing the human heart cDNA library, and the integrated cDNA fragments were isolated from factor-independent Ba/F3 clones by genomic PCR. All cDNA fragments were sequenced and analyzed. Subsequently, a human heart cDNA library in the pME18S vector was screened by using the ^{32}P-labeled cDNA fragment of a clone so as to isolate the entire coding region.

RNA, Protein, and Histological Analyses. Northern blot, *in situ* hybridization, semiquantitative RT-PCR, immunoprecipitation, Western blot, and histological analyses were done as described

Abbreviations: VSMC, vascular smooth muscle cell; TGF, transforming growth factor; EGF, epidermal growth factor; SST, signal sequence trap; SST-REX, retrovirus-mediated SST; CHO, Chinese hamster ovary; RA, retinoic acid; E*n*, embryonic day *n*; LRR, leucine-rich repeat; Ad, adenovirus; Ad-vasorin, Ads expressing vasorin-Flag; PDGF, platelet-derived growth factor.

Data deposition: The sequence reported in this paper has been deposited in the GenBank database (accession no. AY166584).

*To whom correspondence may be addressed at: 4-6-1, Shirokanedai, Minato-ku, Tokyo 108-8639, Japan. E-mail: yikeda-tky@umin.ac.jp or kitamura@ims.u-tokyo.ac.jp.

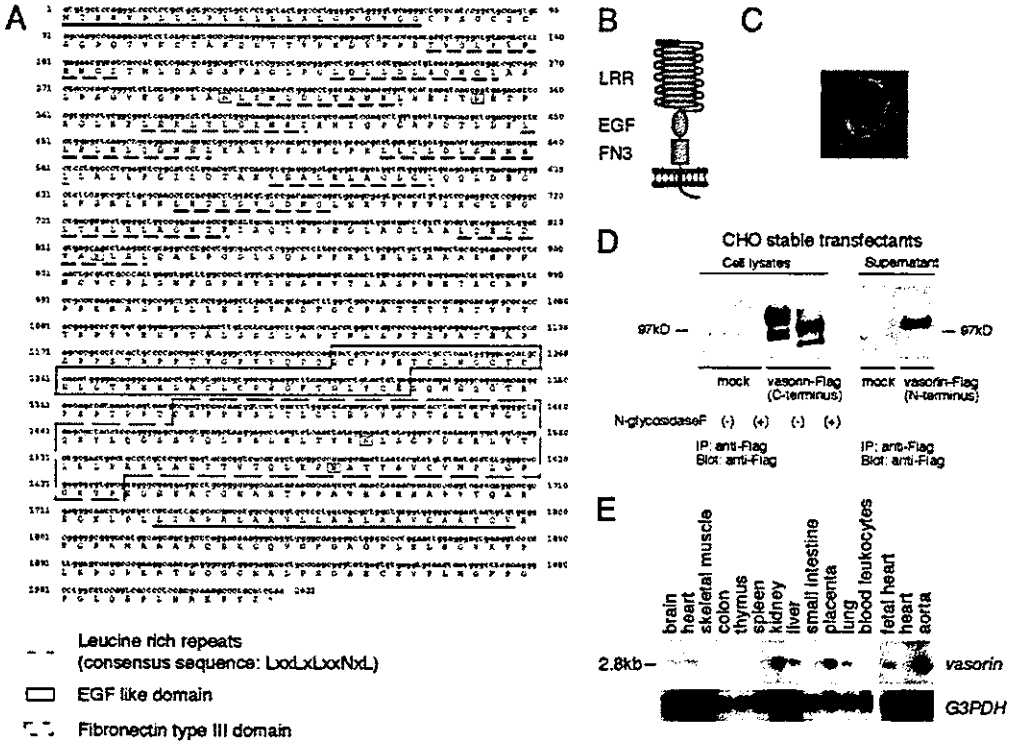

Fig. 1. Vasorin, an identified cell-surface protein. (*A*) Deduced amino acid sequence of human vasorin. The putative signal peptide (underlined), the LRRs (dotted underlines), the EGF motif (boxed), the fibronectin type III motif (dotted boxes), the transmembrane sequence (underlined), and five putative N-glycosylation sites (boxed) are indicated. (*B*) Structural model of vasorin. (*C*) Immunofluorescence analysis of subcellular localization of vasorin. Vasorin was expressed on the cell surface. (*D*) Cell lysates and supernatants of CHO cells stably expressing vasorin-Flag were subjected to immunoprecipitation and Western blot analysis by using an anti-Flag antibody. An ≈110-kDa protein for membrane-bound vasorin with C-terminal tag and a ≈100-kDa protein for soluble vasorin with N-terminal tag were detected under reducing conditions. N-glycosidase F treatment revealed that vasorin is N-glycosylated. (*E*) Northern blot analysis of adult human tissues. A single intense 2.8-kb band was detected and the strongest expression was observed in the aorta.

in *Supporting Text*, which is published as supporting information on the PNAS web site.

Production of the Recombinant Vasorin-Fc Chimera Protein. The bicistronic retroviral vector containing the *vasorin*-Fc chimera, pMX-*vasorin*-Fc chimera-IRES-EGFP, was constructed by inserting the cDNA for the whole-extracellular domain of human *vasorin* and the cDNA for the human Ig Fc region. CHO cells stably expressing the *vasorin*-Fc chimera were expanded in the medium supplemented with 2.5% Ultralow IgG FCS (Invitrogen) and 1% nonessential amino acids (Invitrogen). Secreted recombinant vasorin-Fc chimera protein was purified from the media of infected CHO cells by using Hitrap protein A columns (Amersham Biosciences).

Surface Plasmon Resonance Analysis. The BIAcoreTM2000 system (BIAcore, Uppsala) was used to characterize the interaction and to determine binding characteristics between the recombinant vasorin-Fc and TGF-β1, according to the manufacturer's instructions. To immobilize TGF-β1 on CM5 sensor chips, recombinant human TGF-β1 (R & D Systems) solution in 10 mM acetic acid (pH 4.0) was injected until the desired amount of coupled TGF-β1 was achieved, by using the standard amine-coupling procedure. All experiments were performed at room temperature by using the KINJECT command at a flow rate of 20 μl/min. Responses obtained on control chips were subtracted from those obtained on chips coupled with TGF-β1. Sensorgrams were analyzed by using BIAEVALUATION software (version 3.0).

Transient Transfection and Reporter Assay. CHO stable transfectants were transiently transfected with TGF-β1-responsive luciferase reporter plasmid (p3TP-lux) together with a β-galactosidase reporter plasmid driven by Rous sarcoma virus-LTR as an internal control, by using FuGENE6 (Roche Diagnostics, Roskilde, Denmark). After 24 h, the cells were stimulated for 24 h by adding TGF-β1 (R & D Systems) and were then assayed for luciferase and β-galactosidase activities. Experiments were performed several times and representative data are shown.

Rat Arterial Balloon-Injury Model. Adult rats (weighing 400–450 g) were anesthetized with chloral hydrate (370 mg/kg i.p.). Balloon denudation of the left common carotid artery was done by using a 2F Fogarty catheter (Baxter Edwards Healthcare, Irvine, CA), as described (6). The right common carotid artery served as a control. Rats were killed 3 or 14 days after injury, and the carotid arteries were perfused with 4% paraformaldehyde/PBS. Each injured left carotid artery was excised from the proximal edge of the omohyoid muscle to the carotid bifurcation. The middle third of the segment was isolated for subsequent analyses.

Generation of Recombinant Adenovirus (Ad) Expressing Vasorin. Replication-incompetent Ads expressing vasorin-Flag (Ad-vasorin) were prepared by using the Adeno-X system (Clontech) according to the manufacturer's instructions. Viral titer was measured by end-point dilution assay by using 293 cells.

Statistical Analysis. Quantitative values are expressed as the mean ± SD. Comparisons of means were made by using Student's *t* test for unpaired values; when >2 means were compared, an ANOVA with repeated measurements was used. If a significant *F* value was found, the Scheffé post hoc test for multiple comparisons was used to identify any differences among groups.

Results

Cloning of *Vasorin*. We screened a human heart cDNA library, by using SST-REX (ref. 3 and Table 1, which is published as supporting information on the PNAS web site), and identified a type I membrane protein of 673 aa (Fig. 1*A*). The extracellular region was composed of a putative hydrophobic signal sequence, 10 tandem arrays of a leucine-rich repeat (LRR), an epidermal growth factor (EGF)-like domain, and a fibronectin type III-like domain, and the short intracellular region contained no obvious signaling domain (Fig. 1 *A* and *B*). We termed this protein vasorin, based on the expression pattern described below. By using human vasorin as a probe, we identified homologous mouse and rat protein sequences in the EMBL/GenBank/DDBJ database (accession nos. AK012169 and XM 220168, respectively).

To observe the subcellular localization of vasorin, we stained CHO cells expressing human vasorin-Flag with an anti-Flag antibody (Fig. 1*C*), and confirmed this molecule to be expressed on the cell-surface membrane. Western blotting of cell lysates from CHO stable transfectants revealed a ≈110-kDa protein (Fig. 1*D*), which was larger than the predicted molecular mass. To determine whether this increase in molecular mass was due in part to N-linked glycosylation, immunoprecipitates of vasorin were treated with N-glycosydase F. An apparent shift in molecular mass of vasorin was observed, suggesting that vasorin is a cell-surface glycoprotein (Fig. 1*D*). Next, we examined the supernatant from CHO cells expressing human vasorin-Flag, and soluble vasorin was also detected (Fig. 1*D*).

***Vasorin* Is Predominantly Expressed in VSMCs.** Tissue distribution of *vasorin* was examined by using Northern blot analysis of adult human tissues. The highest expression was detected in the aorta, and moderate expression was detected in the kidney and placenta (Fig. 1*E*). We also performed Northern analysis of various human cell lines. Interestingly, *vasorin* was not expressed abundantly in any cell lines we examined (Fig. 6, which is published as supporting information on the PNAS web site).

To determine the expression pattern of *vasorin* within the aorta, we performed *in situ* hybridization analyses. By using the antisense probe, strong expression of *vasorin* was detected in the tunica media of the proximal ascending aorta (Fig. 2*A*), the descending thoracic aorta (Fig. 2*B*), the abdominal aorta (Fig. 2*C*), and the coronary arteries (Fig. 2 *E* and *F*), suggesting that *vasorin* is expressed in VSMCs of different origins. We also performed *in situ* hybridization analyses in the kidney. *Vasorin* expression was detected in interstitial cells (Fig. 2 *G* and *H*).

Developmental Regulation of *Vasorin* Expression. The developmental regulation of *vasorin* was investigated by using Northern blot and *in situ* hybridization analyses of staged mouse embryos. As shown in Fig. 3*A*, *vasorin* mRNA expression was detected in embryonic day (E)10.5 embryos, with increasing levels of expression observed at subsequent stages (E13.5 and E17.5). With *in situ* hybridization analyses, we examined the expression pattern of *vasorin* during aortic development (Fig. 3*B*). The expression of *vasorin* increased gradually in parallel with the differentiation of VSMCs in aortas at different stages of development (E11.5, E13.5, and E17.5).

When VSMCs are established in culture, a rapid transition from a contractile differentiated phenotype to a synthetic dedifferentiated phenotype occurs (5). To investigate the influence of this phenotypic modulation on the expression of *vasorin*, semiquantitative RT-PCR was performed to compare the expression of *vasorin* in the adult rat aorta with that in cultured rat aortic VSMCs. The expression of *vasorin* was significantly downregulated in the cultured VSMCs (Fig. 3*C*).

P19 embryonal carcinoma cells differentiate into SMCs when given retinoic acid (RA) treatment. Recently, this *in vitro* differentiation system was improved by generating stable cell lines of P19 carrying a smooth muscle α-actin promoter/puromycin resistance gene cassette to enrich SMC lineage cells, by using RA plus puromycin selection. One such stable line, designated as A404, shows a high propensity for SMC differentiation even before puromycin selection (7). As expected, *vasorin* gene expression was induced by RA-treatment in A404 cells (Fig. 3*D*).

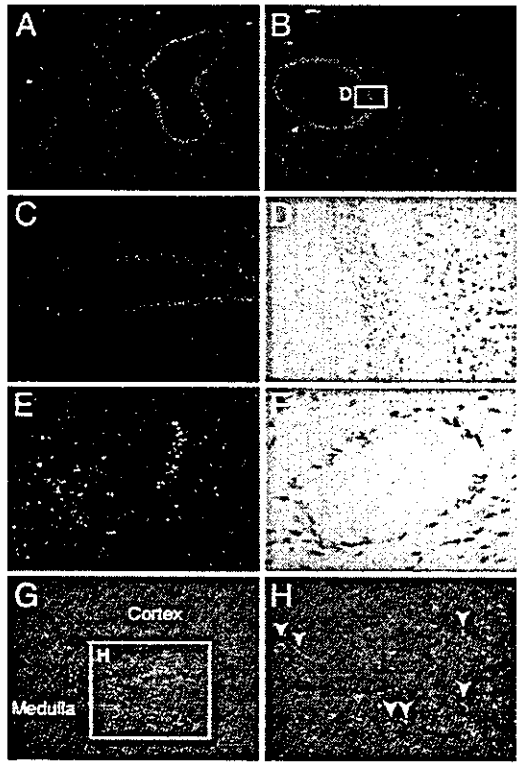

Fig. 2. *In situ* hybridization analysis of *vasorin*. Sections of adult mouse aorta at different levels (*A–D*), the coronary artery (*E* and *F*), and the kidney (*G* and *H*) are shown. *Vasorin* is expressed in VSMCs of different origins. White spots represent hybridization signals. (*A*) The proximal ascending aorta. (*B*) The descending thoracic aorta. (*C*) The abdominal aorta. (*D*) Partial magnification of bright-field image of *B*. Black spots within the elastic fibers represent hybridization signals. (*E*) The coronary artery. (*F*) A bright-field image of the coronary artery. Black spots represent hybridization signals. (*G*) The kidney. (*H*) Partial magnification of *G*. *Vasorin* is expressed in interstitial cells.

Vasorin Directly Binds to TGF-β and Modulates TGF-β Signaling *in Vitro*. An LRR, an EGF-like domain, and a fibronectin type III-like domain are characteristic motifs involved in protein–protein interactions (8). To clarify biological functions of vasorin, we generated recombinant vasorin-Fc fusion protein (Fig. 4*A*), and searched for binding partners of vasorin by using vasorin-Fc as a probe. When comparing the extracellular domain of vasorin with the EMBL/GenBank/DDBJ database, several other LRR protein family members, including decorin, were found to share a significant homology with vasorin. Decorin is a small leucine-rich proteoglycan that interacts directly with TGF-β (9, 10). Considering that vasorin has the same number of LRRs as decorin, and that TGF-β plays an important role in vascular pathophysiology, we tested whether TGF-β binds directly to vasorin. By using a surface plasmon resonance biosensor, we found that the extracellular domain of vasorin directly binds to TGF-β1 in a specific and significant manner (Fig. 4 *B* and *C*). The equilibrium dissociation constant (K_d) was calcu-

Fig. 3. Developmental regulation of *vasorin*. (*A*) Northern blot analysis of staged mouse embryos (E10.5, E13.5, and E17.5). (*B*) Expression pattern of *vasorin* during aortic development examined by *in situ* hybridization analyses. The fourth image is the corresponding bright-field image of the third representation. Arrowheads indicate the aorta in the mouse embryo (E17.5). (*C*) Semiquantitative RT-PCR comparing the expression of *vasorin* in the adult rat aorta with that in cultured rat aortic VSMCs. Rat α-smooth muscle actin (α-SMA) and 18S rRNA were used as a positive and an internal control, respectively. (*D*) Semiquantitative RT-PCR showing the induction of the *vasorin* gene in RA-treated A404 cells. Rat α-SMA and 18S rRNA were used as a positive and an internal control, respectively.

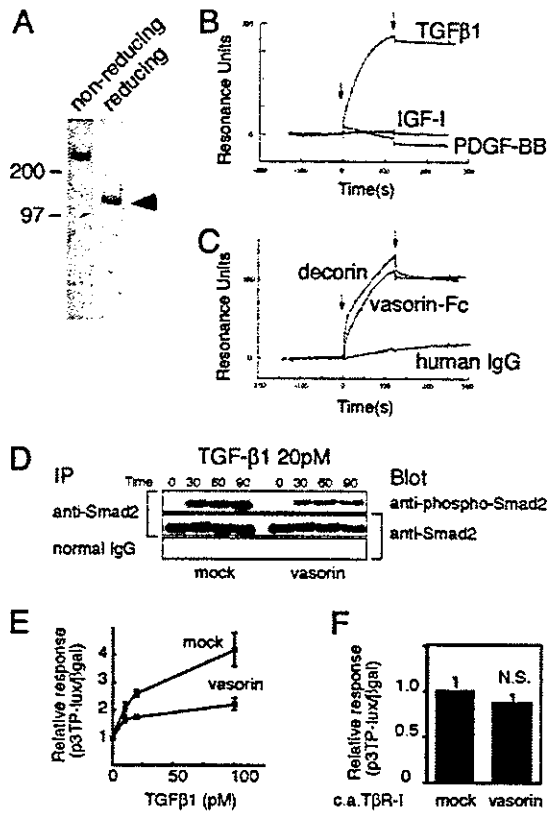

Fig. 4. Vasorin directly binds to TGF-β and modulates TGF-β signaling *in vitro*. (*A*) Purified recombinant vasorin-Fc fusion protein was free of protein contamination, as estimated by SDS/PAGE, followed by Coomassie blue staining. (*B*) Sensorgrams obtained from injection of vasorin-Fc on immobilized TGF-β1, PDGF-BB, and insulin-like growth factor I (IGF-I) are shown. (*C*) Sensorgrams obtained from injection of vasorin-Fc, decorin, and human IgG on immobilized TGF-β1 are shown. Arrowheads indicate initiation and termination of injections. (*D*) TGF-β-induced Smad2 phosphorylation was significantly inhibited in vasorin-expressing cells. Stable transfectants were treated with TGF-β1 (20 pM), and then immunoprecipitated with an anti-Smad2/3 antibody, followed by blotting with an anti-phospho-Smad2 antibody. (*E*) A reporter assay was performed by using the TGF-β-responsive reporter p3TP-lux. Stable transfectants were stimulated with TGF-β1 at various concentrations, and vasorin inhibited TGF-β-induced reporter gene activation. (*F*) Vasorin inhibited TGF-β signaling at the extracellular and/or cell-surface level. The p3TP-lux reporter and the constitutively active TβR-I were cotransfected into stable transfectants. Transfection of the constitutively active TβR-I activated the p3TP-lux reporter, but vasorin did not significantly inhibit this activation. N.S., not significant.

lated to be 0.86 nM. We also tested the binding of TGF-β2 and TGF-β3 to vasorin. TGF-β2 and TGF-β3 showed a specific binding to vasorin with a similar binding affinity to that of TGF-β1 (data not shown).

Next, we examined the functional role of vasorin in TGF-β signaling. First, stable transfectants expressing vasorin were stimulated by TGF-β1 (20 pM). Cells expressing vasorin showed a significant reduction in Smad2 phosphorylation (Fig. 4*D*). Second, we did a reporter assay, by using the TGF-β-responsive reporter p3TP-lux. TGF-β1 activated this reporter in a dose-dependent manner, and vasorin significantly inhibited this effect (Fig. 4*E*). This inhibitory effect of vasorin was specific to TGF-β signaling because vasorin did not affect the cellular responses to irrelevant cytokine stimulation (data not shown). Stable transfectants were also stimulated by using the constitutively active TGF-β type I receptor (constitutively active TβR-I) instead of TGF-β1 stimulation. Transfection of constitutively active TβR-I activated the p3TP-lux reporter, but vasorin did not significantly inhibit this activation (Fig. 4*F*). These findings indicate that vasorin inhibits TGF-β signaling at the extracellular and/or cell-surface level.

Vasorin Expression Was Down-Regulated During Vessel Repair After Arterial Injury, and Reversal of Vasorin Down-Regulation, by Using Ad-Mediated *in Vivo* Gene Transfer, Significantly Reduced Neointimal Formation at Least in Part by Modulating TGF-β Signaling in the Vessel Wall. To investigate *in vivo* functions of vasorin, we used a rat arterial balloon-injury model, because it is a well characterized atherosclerosis model of VSMC-derived lesions, and it is well established that TGF-β contributes to neointimal formation by promoting fibrosis.

Adult rats were subjected to balloon injury with a catheter inserted through the external carotid artery. Vascular injury provokes fibroproliferative activity in quiescent VSMCs, and the phenotypic modulation of VSMCs is induced. Because the fibroproliferative activity of VSMCs peaks at 3 days after injury (6), balloon-injured carotid arteries were harvested at 3 days after insertion to examine the expression levels of *vasorin* by semiquantitative RT-PCR. Consistent with our findings described above (Fig. 3 *A–D*), down-regulation of *vasorin* expression was induced by mechanical vascular injury (Fig. 5*A*). In contrast, the expression of several cytokines, including TGF-β, was up-regulated by vascular injury, and the ratio of TGF-β to vasorin was increased (Fig. 5*A*).

Next, we investigated the functional role of vasorin down-regulation in neointimal formation. To restore *vasorin* expression during vessel repair after injury, we did Ad-mediated *vasorin* gene transfer to balloon-injured rat carotid arteries. Replication-defective Ad-vasorin were constructed, and after denudation with a balloon catheter, the vessel wall was exposed to the adenoviral solution (1×10^9 pfu) for 20 min to deliver *vasorin* gene locally. First, arteries were harvested 3 days after-